

A BENAMOU–BRENIER PROXIMAL SPLITTING METHOD FOR CONSTRAINED UNBALANCED OPTIMAL TRANSPORT

MAO NISHINO , MARTIN BAUER , TOM NEEDHAM *, AND NICOLAS CHARON †

Abstract. The dynamic formulation of optimal transport, also known as the Benamou-Brenier formulation, has been extended to the unbalanced case by introducing a source term in the continuity equation. When this source term is penalized based on the Fisher-Rao metric, the resulting model is referred to as the Wasserstein-Fisher-Rao (WFR) setting, and allows for the comparison between any two positive measures without the need for equalized total mass. In recent work we introduced a constrained variant of this model, in which affine integral equality constraints are imposed along the measure path. In the present paper, we propose a further generalization of this framework, which allows for constraints that apply not just to the density path but also to the momentum and source terms, and incorporates affine inequalities in addition to equality constraints. We prove, under suitable assumptions on the constraints, the well-posedness of the resulting class of convex variational problems. The paper is then primarily devoted to developing an effective numerical pipeline that tackles the corresponding constrained optimization problem based on finite difference discretizations and parallel proximal schemes. Our proposed framework encompasses standard balanced and unbalanced optimal transport, as well as a multitude of natural and practically relevant constraints, and we highlight its versatility via several synthetic and real data examples.

1. Introduction. Optimal transport (OT) is a powerful mathematical framework for comparing probability distributions over a fixed metric space [Vi09, PC⁺19]. Classical formulations focus on the Wasserstein distances, a family of metrics that compare probability measures while incorporating the geometry of the underlying space. The theory of unbalanced optimal transport (UOT) generalizes this framework by enabling the comparison of positive measures of potentially different total masses [CPSV18a, CPSV18b, PR14, LMS16, LMS18]. This flexibility is particularly useful in applications where differences in total population are important; for example, UOT has applications to the modeling of cell population dynamics [SST⁺19], image processing and color transfer [NNZN23], crowd counting [MWH⁺21] and domain adaptation in machine learning [FSFC21]. Moreover, UOT can be useful even when total population differences are not explicitly important, as the ability to create or destroy mass leads to improved robustness to outlier noise [SFV⁺19, WSZJ24]. Intuitively, the dynamic formulation of UOT expands on the Benamou-Brenier characterization of classical OT [BB00], thereby achieving the comparison of two measures by joining them via a path in the space of measures which minimizes a certain kinetic energy functional. From this perspective, it is natural in applications that one may wish to impose additional constraints on the mass transport path. For example, in population dynamics modeling, one may have knowledge of the total population over time, which can be formulated as a total mass constraint over the transport path. A particular instance of this constraint is that the total mass should remain constant while still allowing for local mass creation/destruction; this leads to the spherical Hellinger-Kantorovich (SHK) metric framework, introduced in [LM19] and implemented via a deep learning approach in [JCLL24], with applications to generative sampling. Alternatively, one may wish to constrain the spatial characteristics of measure trajectories in the UOT framework. For example, applications to robotics [DJH⁺25] require the modeling of obstacles in the environment which must be avoided along trajectories. As a final example, when describing crowd motion [BJO09, MRS10, KBAH13, ROL⁺20], limiting congestion can be modeled via different types of constraints, one of which being to upper bound the density in a particular region. Inspired by the potential applications described above, a constrained unbalanced optimal transport model was considered in our previous work [BCNN25], where we studied the theoretical aspects of the UOT problem with affine constraints on the mass density; we will refer to this framework as ACUOT, which stands for affine-constrained unbalanced optimal transport. To provide an informal overview of our formulation in [BCNN25], let $\Omega \subset \mathbb{R}^n$ be a compact domain and let ρ_0, ρ_1 be two positive densities on Ω . In dynamic UOT, one considers a path of densities $\rho : [0, 1] \times \Omega$, a path of momentum vector fields $\omega : [0, 1] \times \Omega \rightarrow \mathbb{R}^n$ (describing the transport dynamics), and a path of source terms $\zeta : [0, 1] \times \Omega \rightarrow \mathbb{R}$ (capturing the creation or destruction of mass). Given a balance parameter $\delta \geq 0$, the UOT problem then seeks to minimize the Wasserstein-Fisher-Rao energy [CPSV18a]

$$(1.1) \quad \int_0^1 \int_{\Omega} \frac{\|\omega(t, x)\|^2 + \delta^2 \zeta(t, x)^2}{2\rho(t, x)} dx dt,$$

*Department of Mathematics, Florida State University, Tallahassee, FL 32306, USA (mnishino@fsu.edu, mbauer2@fsu.edu, tneedham@fsu.edu).

†Department of Mathematics, University of Houston, Houston, TX 77204, USA (ncharon@central.uh.edu).

subject to the continuity equation

$$(1.2) \quad \partial_t \rho + \nabla \cdot \omega = \zeta,$$

over all triples (ρ, ω, ζ) satisfying the given initial data $\rho(0, \cdot) = \rho_0$, $\rho(1, \cdot) = \rho_1$. In the ACUOT problem, we additionally introduce an affine constraint on the density path

$$(1.3) \quad \int_{\Omega} H(t, x) \rho(t, x) dx = F(t) \quad \text{for a.e. } t \in [0, 1],$$

where $H : [0, 1] \times \Omega \rightarrow \mathbb{R}^d$ and $F : [0, 1] \rightarrow \mathbb{R}^d$ are given functions that define the affine constraint. In this formulation, the main contribution of [BCNN25] was to show the existence of minimizers for the ACUOT problem under suitable technical assumptions on the constraint functions H and F . However, the above formulation lacks two important generalizations that are relevant in practice. First, the constraints are only imposed on the density path ρ , whereas it is natural in certain applications to impose constraints on the control variables as well; e.g., in modeling population dynamics, we may want to restrict the growth rate of the population (source term, ζ) or limit the direction of mass movement (momentum, ω). Second, the constraints are only affine integral equalities, while one may wish to instead impose inequality constraints; e.g., upper bounding the total population over time. Lastly, [BCNN25] only focused on the theoretical aspects of the model, such as the well-posedness of the corresponding variational problems, but did not address the numerical solution to the ACUOT problem in practice.

1.1. Main contributions. The goal of this paper is to address the limitations of the ACUOT model described above. Our main contributions are described as follows. **Generalized constrained UOT model.** Including the control terms, we generalize the ACUOT model of [BCNN25] by considering the UOT problem described by (1.1) and (1.2), but with additional constraints of a form more general than (1.3). Namely, for $i = 1, \dots, d$, we impose

$$\begin{aligned} \int_{\Omega} H_i^{\rho}(t, x) \rho(t, x) dx + \int_{\Omega} H_i^{\omega}(t, x) \cdot \omega(t, x) dx \\ + \int_{\Omega} H_i^{\zeta}(t, x) \zeta(t, x) dx \leq F_i(t) \quad \text{for a.e. } t \in [0, 1]. \end{aligned}$$

Here, $(H_i^{\rho}, H_i^{\omega}, H_i^{\zeta}) : [0, 1] \times \Omega \rightarrow \mathbb{R} \times \mathbb{R}^n \times \mathbb{R}$ are given functions that define the constraints on the density, momentum and source term, respectively, and $F_i : [0, 1] \rightarrow \mathbb{R}$ is a given function that defines the bounds on the affine functional. A formal definition of this extended model is given in Section 3. The main contribution of this part of the article can be found in Theorem 3.4, where we show the existence of minimizers for this generalized constrained UOT problem under suitable technical assumptions on the constraint functions $H_i^{\rho}, H_i^{\omega}, H_i^{\zeta}$ and F . **A discrete model.** To develop a numerical method for solving the generalized constrained UOT problem, we first discretize its associated energy. This is achieved by employing a standard grid on the time–space domain $[0, 1] \times \Omega$ and using finite-difference schemes to approximate the continuity equation. We then show in Theorem 4.1, that the resulting discrete problem admits minimizers, under suitable assumptions, just as in the continuous setting. **Numerical framework for the generalized model.** Finally, we use the above described discretization to develop a parallelizable numerical framework for solving the generalized constrained UOT problem. To make use of the convexity of the problem, we employ a convex optimization approach to solve the resulting discrete problem. In particular, we use the proximal splitting algorithm as done by [CPSV18a] but rely on the parallel proximal algorithm [CP08, CP11] instead of the Douglas-Rachford algorithm used in the previous work. This algorithm allows us to incorporate multiple constraints easily and to parallelize the computation of the proximal operators. The previously obtained existence results for the discretized energy can be used to show the convergence of the algorithm, cf. Remark 4.2. Finally we demonstrate the versatility of our numerical framework on several synthetic examples as well as real-world data on population dynamics.

1.2. Relationship to existing literature. We first re-emphasize that the present paper deals with constraints for dynamic OT, in contrast with other lines of work which have instead introduced constraints on the transport plans in the static Kantorovich setting, such as capacity constraints [KM15, TRS⁺24],

martingale constraints [ES18, DS14], or constraints designed to handle Gaussian mixtures [DD20, WNP⁺23]. Several past works have considered different constraints within dynamic formulations of optimal transport and proposed numerical approaches for such problems, although primarily in the balanced setting [PPO14, WZB⁺23, KN22, WR24]. In the unbalanced case, [JCLL24] develops a deep-learning-based algorithm for the specific SHK model. For more general constraints, [NBT⁺24] and [WPZ⁺24] both propose algorithms based on neural network architectures and with soft constraints enforced via penalty terms. All these works are geared towards applications to flow matching and sampling problems in high dimension, and, despite arguably being scalable for such purposes, they typically fall out of the convex problems and optimization landscape, thus lacking clear theoretical convergence guarantees. Our work, on the other hand, focuses on a particular family of hard constraints—namely, affine integral equality/inequality constraints—which preserve the convexity of the original formulation of UOT. This allows us to provide conditions for the well-posedness of the resulting variational problems, and leverage convex optimization to derive a numerical solver with actual convergence properties. However, this makes the proposed approach better suited for optimal transport of density measures on low-dimensional domains.

1.3. Outline of the paper. The structure of the paper is as follows. In Section 2, we give a brief review of the theoretical perspective on the unbalanced optimal transport problem and the constrained model of [BCNN25]. Section 3 introduces the generalized constrained model and includes the main existence theorem. We present our numerical framework to solve the generalized constrained UOT problem in Section 4. In Section 5, we provide examples of applications to our numerical algorithm to both synthetic and real-world data. The paper concludes with a short discussion of potential future research directions in Section 6. Proofs of theoretical results and additional algorithmic and experimental details are included in the Supplementary Material.

2. Background: Dynamic Optimal Transport and the Wasserstein-Fisher-Rao metric. In this section, we will give a brief review of dynamic (unbalanced) optimal transport and, in particular, of the constrained model introduced in [BCNN25]. For more details we refer to [BCNN25, Section 2 and 3], from which the notation and most of the definitions of this section are taken.

2.1. Dynamic optimal transport and the Wasserstein distance. From here on let $\Omega \subset \mathbb{R}^n$ denote a fixed compact set with C^1 boundary and let ρ_0 and ρ_1 be probability measures on Ω . To simplify the presentation we assume that each of the measures ρ_i has density $u_i : \Omega \rightarrow \mathbb{R}$ with respect to the Lebesgue measure on \mathbb{R}^n . In this setting, the Benamou-Brenier formulation [BB00] of optimal transport consists of the optimization problem

$$(2.1) \quad \inf_{u,v} \int_0^1 \int_{\Omega} \frac{\|v(t,x)\|^2}{u(t,x)} dx dt,$$

where the infimum is taken over all paths of densities $u : [0,1] \times \Omega \rightarrow \mathbb{R}$ and time-dependent vector fields $v : [0,1] \times \Omega \rightarrow \mathbb{R}^n$ subject to the **continuity equation**

$$(2.2) \quad \partial_t u + \nabla \cdot v = 0, \quad u(0, \cdot) = u_0, \quad u(1, \cdot) = u_1.$$

The seminal results of Benamou and Brenier [BB00] state that this formulation of optimal transport is equivalent to the standard Kantorovich formulation and thus the square root of the optimal energy is the so-called **Wasserstein distance**. Note that this formulation directly leads to a (formal) Riemannian interpretation of the Wasserstein-distance, where the corresponding energy Lagrangian is given by (2.1); the corresponding (formal) Riemannian metric is often called the **Otto metric** [Ott01].

2.2. The Fisher-Rao metric and the Hellinger distance. Another approach to metrizing the space of (probability) densities is given by the Hellinger distance, which has its origins in the field of information geometry [Ama16]. It is the geodesic distance of a Riemannian metric called the Fisher-Rao metric and was originally introduced to compare elements of finite-dimensional submanifolds of probability densities in the context of statistics [RR45], but has since then been extended to the infinite dimensional setting; see, e.g., [Fri91, AJVLS17, BBM16]. While the Wasserstein distance (Otto metric, respectively) is defined for probability densities, the Hellinger distance (Fisher-Rao metric, respectively) can be naturally defined on the space of all densities (without a mass preservation constraint). To define this distance, we restrict ourselves

to the space of all measures ρ that have a positive density $u : \Omega \rightarrow \mathbb{R}_{>0}$ with respect to the Lebesgue measure. Given two such densities $u_0, u_1 : \Omega \rightarrow \mathbb{R}$, the **Hellinger distance** between them is given by

$$(2.3) \quad \inf_{u,w} \int_0^1 \int_{\Omega} \frac{w(t,x)^2}{u(t,x)} dx dt,$$

where the infimum is over sufficiently smooth paths of densities $u : [0,1] \times \Omega \rightarrow \mathbb{R}$ and functions $w : [0,1] \times \Omega \rightarrow \mathbb{R}$, subject to the **continuity equation**

$$(2.4) \quad \partial_t u = w, \quad u(0, \cdot) = u_0, \quad u(1, \cdot) = u_1.$$

Note that the energy Lagrangian (2.3) is again quadratic and thus it implicitly defines a Riemannian metric on the space of positive densities; this is exactly the **Fisher-Rao metric**.

2.3. Unbalanced dynamic optimal transport and the Wasserstein-Fisher-Rao distance. In the *unbalanced optimal transport* framework [CPSV18a], the approaches described above (dynamic optimal transport and Fisher-Rao geometry) are combined to define a new metric on the space of all densities. The main idea behind this framework is to combine the continuity equations of optimal transport and information geometry to obtain

$$(2.5) \quad \partial_t u + \nabla \cdot v = w,$$

where $w : [0,1] \times \Omega \rightarrow \mathbb{R}$ is interpreted as a source term, which allows the creation and destruction of mass, and where $\nabla \cdot v$ is the transport term. When expressed in the form (2.5) ((2.2) or (2.4), respectively), the continuity equation inherently assumes that the measure ρ admits a differentiable density. As shown in [CPSV18a], this requirement can be relaxed by instead formulating the equation in its weak (distributional) sense. To introduce the Wasserstein-Fisher-Rao Lagrangian, which serves as the basis of the constrained model studied in this article, we will first recall this notion in the following definition.

DEFINITION 2.1 (Distributional Continuity Equation). *Let $\rho_0, \rho_1 \in \mathcal{M}^+(\Omega)$. We say that a triple $(\rho, \omega, \zeta) \in \mathcal{M}^+([0,1] \times \Omega) \times \mathcal{M}([0,1] \times \Omega)^n \times \mathcal{M}([0,1] \times \Omega)$ satisfies the **continuity equation in the distributional sense** with boundary conditions ρ_0 and ρ_1 if, for any $\phi \in C^1([0,1] \times \Omega)$,*

$$\int_{[0,1] \times \Omega} \partial_t \phi d\rho + \int_{[0,1] \times \Omega} \nabla \phi \cdot d\omega + \int_{[0,1] \times \Omega} \phi d\zeta = \int_{\Omega} \phi(1, \cdot) d\rho_1 - \int_{\Omega} \phi(0, \cdot) d\rho_0$$

We denote by $\mathcal{CE}(\rho_0, \rho_1)$ the set of triples (ρ, ω, ζ) satisfying the continuity equation with boundary conditions ρ_0, ρ_1 .

The unbalanced optimal transport distance of [CPSV18a] is then defined as follows.

DEFINITION 2.2 (WFR distance). *For $\delta > 0$, the **Wasserstein-Fisher-Rao infinitesimal cost** is the function $f_{\delta} : \mathbb{R} \times \mathbb{R}^n \times \mathbb{R} \rightarrow [0, +\infty]$ defined by*

$$f_{\delta}(\rho, \omega, \zeta) := \begin{cases} \frac{\|\omega\|^2 + \delta^2 \zeta^2}{2\rho}, & \rho > 0 \\ 0, & (\rho, \omega, \zeta) = (0, 0, 0) \\ +\infty, & \text{otherwise.} \end{cases}$$

The associated **Wasserstein-Fisher-Rao (WFR) distance** is then defined by

$$(2.6) \quad \text{WFR}_{\delta}(\rho_0, \rho_1)^2 := \inf \left\{ \int_{[0,1] \times \Omega} f_{\delta} \left(\frac{d\mu}{d\lambda} \right) d\lambda \mid \mu = (\rho, \omega, \zeta) \in \mathcal{CE}(\rho_0, \rho_1) \right\},$$

where λ is any nonnegative measure on $[0,1] \times \Omega$ such that $\rho, \omega, \zeta \ll \lambda$ and $\frac{d\mu}{d\lambda} := (\frac{d\rho}{d\lambda}, \frac{d\omega}{d\lambda}, \frac{d\zeta}{d\lambda})$. We note that the value does not depend on the choice of λ due to the 1-homogeneity of f_{δ} , cf. [BCNN25, Definition 2.2].

Remark 2.3. Considering ρ as an element of $\mathcal{M}^+([0,1] \times \Omega)$, one loses the dynamical interpretation of ρ as a “path of measures”, but this interpretation is recovered via the concept of disintegration, i.e., one can **disintegrate** the measure ν on $[0,1] \times \Omega$ as a Borel family of measures $\{\nu_t\}_{t \in [0,1]}$ such that $d\nu(t, x) = dt \otimes d\nu_t(x)$; cf. [BCNN25, Proposition 2.4]. In the following, we will write in short $\nu = dt \otimes \nu_t$ and we will frequently abuse terminology and refer to μ, ρ, ω , and ζ as *paths of measures*, or simply as *paths*.

2.4. Constrained unbalanced dynamic optimal transport. Finally, we revisit the constrained, unbalanced optimal transport framework introduced in our earlier work [BCNN25]. This framework will then be broadened and generalized in the subsequent sections of this article. The idea of the constrained model of [BCNN25] was to restrict the set of admissible paths in the dynamic formulation of unbalanced optimal transport to satisfy certain (time dependent) integral constraints on the densities ρ . The full model is introduced in the following definition:

DEFINITION 2.4 (WFR problem with time-varying constraints). *For functions $H : [0, 1] \times \Omega \rightarrow \mathbb{R}^d$ and $F : [0, 1] \rightarrow \mathbb{R}^d$, we say that a measure $\rho \in \mathcal{M}^+([0, 1] \times \Omega)$ **satisfies an affine constraint** with respect to H and F if it disintegrates in time ($\rho = dt \otimes \rho_t$) and*

$$\int_{\Omega} H(t, x) d\rho_t(x) = F(t) \quad \text{for a.e. } t \in [0, 1].$$

In this case, we write $\rho \in \mathcal{A}(H, F)$. For $\rho_0, \rho_1 \in \mathcal{M}^+(\Omega)$, we consider the constrained set of measures

$$(2.7) \quad \mathcal{CE}_{H,F}(\rho_0, \rho_1) := \{\mu = (\rho, \omega, \zeta) \in \mathcal{CE}(\rho_0, \rho_1) \mid \rho \in \mathcal{A}(H, F)\}.$$

We define the **Wasserstein-Fisher-Rao energy with time-varying affine constraints** by

$$(2.8) \quad WFR_{\delta}^{H,F}(\rho_0, \rho_1)^2 = \inf \left\{ \int_{[0,1] \times \Omega} f_{\delta} \left(\frac{d\mu}{d\lambda} \right) d\lambda \mid \mu = (\rho, \omega, \zeta) \in \mathcal{CE}_{H,F}(\rho_0, \rho_1) \right\},$$

where λ is any nonnegative Borel measure on $[0, 1] \times \Omega$ such that $\rho, \omega, \zeta \ll \lambda$. By the homogeneity of f_{δ} , the integral in the definition does not depend on the choice of λ .

Remark 2.5. If the constraints do not depend on time, i.e., $H(t, x) = H(x)$ and $F(t) = C > 0$, then one can view the constrained Wasserstein-Fisher-Rao energy as an energy Lagrangian on the constrained space of measures

$$\mathcal{M}_{H,C}^+(\Omega) := \left\{ \rho \in \mathcal{M}^+(\Omega) \mid \int_{\Omega} H d\rho = C \right\},$$

and, under additional assumptions on H , this defines a distance function on this constrained space of measures, cf. [BCNN25, Theorem 3.8].

The main result of our previous article [BCNN25] established the existence of minimizers to (2.8) assuming that the problem is feasible, i.e., assuming that there exist finite energy paths that satisfy the constraints, cf. [BCNN25, Theorem 4.3]. In the next section, we will significantly broaden this constrained model by allowing constraints not only on the density path, but also on the paths of controls. The main theoretical result of the present article will then show the existence of minimizers for this extended model.

3. Generalized Model for Constrained Unbalanced Optimal Transport. In this section, we aim to introduce a generalization of the constrained model of [BCNN25], as presented in Section 2.4. We are specifically interested in generalizing the allowable constraints in two different directions, while preserving the convexity properties of the resulting variational problems:

1. We will consider constraints that operate on the control variables (ω, ζ) , in addition to the density ρ .
2. We will allow constraints that involve affine inequalities instead of just equalities.

This section formalizes this extended framework and generalizes the main existence result of [BCNN25] to this setting.

3.1. Generalized constraint model. We begin by introducing a new constrained space of measure triplets

$$(\rho, \omega, \zeta) \in \mathcal{M}^+([0, 1] \times \Omega) \times \mathcal{M}([0, 1] \times \Omega)^n \times \mathcal{M}([0, 1] \times \Omega).$$

DEFINITION 3.1. *Given functions $F : [0, 1] \rightarrow \mathbb{R}$, $H^{\rho} : [0, 1] \times \Omega \rightarrow \mathbb{R}$, $H^{\omega} : [0, 1] \times \Omega \rightarrow \mathbb{R}^n$, and $H^{\zeta} : [0, 1] \times \Omega \rightarrow \mathbb{R}$, letting $H = (H^{\rho}, H^{\omega}, H^{\zeta})$, we say that $\mu = (\rho, \omega, \zeta)$ belongs to the **affine equality***

constraint space $\mathcal{A}^{eq}(H, F)$ if the three measures ρ, ω and ζ disintegrate in time ($\rho = dt \otimes \rho_t$, $\omega = dt \otimes \omega_t$, and $\zeta = dt \otimes \zeta_t$) and

$$\int_{\Omega} H^{\rho}(t, x) d\rho_t(x) + \int_{\Omega} H^{\omega}(t, x) \cdot d\omega_t(x) + \int_{\Omega} H^{\zeta}(t, x) d\zeta_t(x) = F(t) \text{ for a.e. } t \in [0, 1].$$

Similarly, we say that $\mu = (\rho, \omega, \zeta)$ belongs to the **affine inequality constraint space** $\mathcal{A}^{ineq}(H, F)$ if the three measures ρ, ω and ζ disintegrate in time and

$$\int_{\Omega} H^{\rho}(t, x) d\rho_t(x) + \int_{\Omega} H^{\omega}(t, x) \cdot d\omega_t(x) + \int_{\Omega} H^{\zeta}(t, x) d\zeta_t(x) \leq F(t) \text{ for a.e. } t \in [0, 1].$$

We can now introduce a generalized version of the constrained unbalanced optimal transport problem as follows.

DEFINITION 3.2. For $d \in \mathbb{N}$ consider functions $H_i = (H_i^{\rho}, H_i^{\omega}, H_i^{\zeta}) : [0, 1] \times \Omega \rightarrow \mathbb{R} \times \mathbb{R}^n \times \mathbb{R}$ and $F_i : [0, 1] \rightarrow \mathbb{R}$, for $i = 1, \dots, d$. For $\rho_0, \rho_1 \in \mathcal{M}^+(\Omega)$, and another integer d' such that $0 \leq d' \leq d$, we define the **set of constrained paths** from ρ_0 to ρ_1 by

$$\begin{aligned} \mathcal{CE}_{H,F}(\rho_0, \rho_1) = \{ \mu \in \mathcal{CE}(\rho_0, \rho_1) \mid & \mu \in \mathcal{A}^{ineq}(H_i, F_i) \text{ for } i = 1, \dots, d', \text{ and} \\ & \mu \in \mathcal{A}^{eq}(H_i, F_i) \text{ for } i = d' + 1, \dots, d \}. \end{aligned}$$

Note that, with a slight abuse of notation, we recycle notation from (2.7) and we suppress the dependency in the index d' , both for the sake of simplicity. We then define the **Wasserstein-Fisher-Rao energy** with the affine inequality and equality constraints given by H and F similar to (2.6) (once again recycling notation):

$$(3.1) \quad WFR_{\delta}^{H,F}(\rho_0, \rho_1)^2 = \inf \left\{ \int_{[0,1] \times \Omega} f_{\delta} \left(\frac{d\mu}{d\lambda} \right) d\lambda \mid \mu = (\rho, \omega, \zeta) \in \mathcal{CE}_{H,F}(\rho_0, \rho_1) \right\}.$$

In other words, (3.1) corresponds to minimizing the Wasserstein-Fisher-Rao cost over paths μ that satisfy a set of d' integral affine inequality constraints and $d - d'$ integral affine equality constraints.

Remark 3.3. Note that we can recover the setting of [BCNN25], as described in Section 2.4, by restricting to spaces \mathcal{A}^{eq} in which $d' = 0$ and $H_i^{\omega} = 0$, $H_i^{\zeta} = 0$ for all $i = 1, \dots, d$. On the other hand, setting $H^{\rho} = 0$ leads to constraints that only operate on the control measures ω and ζ .

3.2. Existence of minimizers. We may now generalize the optimal path existence result [BCNN25, Theorem 4.3] to this new setting.

THEOREM 3.4. Let $\rho_0, \rho_1 \in \mathcal{M}^+(\Omega)$ and $H : [0, 1] \times \Omega \rightarrow (\mathbb{R} \times \mathbb{R}^n \times \mathbb{R})^d$, $F : [0, 1] \rightarrow \mathbb{R}^d$ be continuous functions. If the problem (3.1) is feasible, i.e., there exists $\mu \in \mathcal{CE}_{H,F}(\rho_0, \rho_1)$ with finite WFR cost, then an optimal path exists.

The proof of this Theorem, which is postponed to Supplementary Material C.1, follows a similar proof strategy as in [BCNN25], based again on the use of the Fenchel-Rockafellar theorem (see [BZ05]). While the overall strategy is the same, this generalized setting requires more detailed analysis to handle the inequality constraints.

Remark 3.5 (Feasibility of the constrained problem). In order to obtain the real existence of minimizers to (3.1), one still needs the problem to be *feasible* in the sense that there exists a finite energy path in $\mathcal{CE}_{H,F}(\rho_0, \rho_1)$. For the more restricted constrained model discussed in Section 2.4, this can be shown for several classes of constraints, cf. [BCNN25, Theorems 3.5, 4.7 and 4.6]. For the more general model considered in this article, a comprehensive result regarding feasibility seems out of reach due to the increased technicality of this question in this extended context. However, for the specific examples presented in Section 5, the feasibility always holds. Indeed, in the experiments of Sections 5.1, 5.2, 5.3 and 5.5, this is guaranteed by the results of [BCNN25, Theorems 4.6 and 4.7]. For the example of Section 5.4.1, it also holds as the constraint is only on the momentum variable ω and thus a pure Fisher-Rao geodesic (with no transport) gives rise to a finite energy path satisfying the constraints. Lastly, for the example studied in Section 5.4.2, which involves constraints on the source term ζ , the feasibility follows by constructing a transport path and combining this with adapting the total mass using the source term ζ in regions where the constraint function H^{ζ} is zero.

4. Discrete problem and algorithmic approach. In order to derive a numerical approach to tackle the constrained UOT model of Section 3, with provable convergence guarantees, we shall adapt the algorithm of [CPSV18a] in the unconstrained setting, which is itself based on the Douglas-Rachford (DR) splitting scheme [DR56, GM75]. In the following sections, we will describe the chosen discretization in more detail, as well as our proposed numerical framework; pseudocode for the algorithm can be found in Supplementary Material B and an open source implementation is available at our GitHub repository: <https://github.com/mao1756/acuot>.

4.1. Discretized problem. Throughout this section, we consider the time domain to be $[0, 1]$ and the space domain Ω to be $\Omega = [0, L]$ where L is the length of the domain in the spatial dimension. We consider the 0th dimension as the time dimension and the 1st dimension as the spatial dimension. Furthermore, letting N_0, N_1 be the number of discretization steps in time and space, respectively, we shall use uniform discretization steps of the form $h_0 = 1/N_0$ and $h_1 = L/N_1$. We first consider the discretization of the domain. Rather than discretizing all continuous variables (ρ, ω, ζ) of the variational problem on a single time-space grid, we will consider, following the idea first proposed in [PPO14], two types of grids: namely, a centered grid and staggered grids, where staggered grids are shifted by half a cell in a particular dimension. Specifically, the centered grid \mathcal{G}_c is defined as

$$\mathcal{G}_c = \left\{ (t_{j_0}, x_{j_1}) : t_{j_0} = \frac{j_0 + \frac{1}{2}}{N_0}, x_{j_1} = \frac{(j_1 + \frac{1}{2})L}{N_1} \right\}$$

while the staggered grids for time and space dimensions are then given respectively by:

$$\begin{aligned} \mathcal{G}_s^t &= \left\{ (t_{j_0}, x_{j_1}) : t_{j_0} = \frac{j_0}{N_0}, x_{j_1} = \frac{(j_1 + \frac{1}{2})L}{N_1}, j_0 \in \llbracket 0, N_0 \rrbracket, j_1 \in \llbracket 0, N_1 - 1 \rrbracket \right\}, \\ \mathcal{G}_s^x &= \left\{ (t_{j_0}, x_{j_1}) : t_{j_0} = \frac{j_0 + \frac{1}{2}}{N_0}, x_{j_1} = \frac{j_1 L}{N_1}, j_0 \in \llbracket 0, N_0 - 1 \rrbracket, j_1 \in \llbracket 0, N_1 \rrbracket \right\}. \end{aligned}$$

We shall then consider centered variables $V = (\rho, \omega, \zeta) \in \mathcal{E}_c := \mathbb{R}^{\mathcal{G}_c} \times \mathbb{R}^{\mathcal{G}_c} \times \mathbb{R}^{\mathcal{G}_c}$ where each of the three components is defined on the centered grid, as well as staggered variables $U = (\bar{\rho}, \bar{\omega}, \bar{\zeta}) \in \mathcal{E}_s := \mathbb{R}^{\mathcal{G}_s^t} \times \mathbb{R}^{\mathcal{G}_s^x} \times \mathbb{R}^{\mathcal{G}_c}$ where the density and momentum field are sampled on the corresponding staggered grids. With a slight abuse of notations, we will write $\rho_{j_0, j_1}, \omega_{j_0, j_1}, \zeta_{j_0, j_1}$ to denote the values of ρ, ω and ζ sampled at $(t_{j_0}, x_{j_1}) \in \mathcal{G}_c$ and similarly for the staggered variables $\bar{\rho}, \bar{\omega}, \bar{\zeta}$. The idea behind the use of these different types of grids and variables is that it will provide a more natural way to evaluate the discrete derivatives involved in the continuity equation, as explained in the next subsection. Note that the source term is always defined on the centered grid since no derivative of ζ is involved in the problem formulation. One can convert a staggered variable to a centered variable via the interpolation operator $I : \mathcal{E}_s \rightarrow \mathcal{E}_c$ which is defined as $I(U) = (I_\rho \bar{\rho}, I_\omega \bar{\omega}, \bar{\zeta})$ where

$$\begin{aligned} (I_\rho \bar{\rho})_{j_0, j_1} &= \frac{1}{2}(\bar{\rho}_{j_0, j_1} + \bar{\rho}_{j_0+1, j_1}), \\ (I_\omega \bar{\omega})_{j_0, j_1} &= \frac{1}{2}(\bar{\omega}_{j_0, j_1} + \bar{\omega}_{j_0, j_1+1}) \end{aligned}$$

This allows us to then define the consistency condition between the staggered and centered representations as $V = I(U)$. We note that the above definitions can be easily modified for periodic boundary conditions (in space), by simple cyclic wrapping of the indices. Based on the previous definitions, we now examine the discretization of the continuity equation $\partial_t \rho + \text{div } \omega = \zeta$. First, we define the time-space divergence operator $\text{div} : \mathcal{E}_s \rightarrow \mathbb{R}^{\mathcal{G}_c}$ is defined by forward face-to-cell differences:

$$(\text{div } U)_{j_0, j_1} = \frac{\bar{\rho}_{j_0+1, j_1} - \bar{\rho}_{j_0, j_1}}{h_0} + \frac{\bar{\omega}_{j_0, j_1+1} - \bar{\omega}_{j_0, j_1}}{h_1}.$$

The discrete continuity equation can then be written as $(\text{div} - s_z)(U) = 0$ where s_z is the auxiliary operator that extracts the source term from a staggered variable, i.e. $s_z(U) = \bar{\zeta}$. In addition, one also needs to enforce the initial and terminal conditions on the density as well as the no-flux (Neumann) spatial boundary conditions on the momentum. To this end, we introduce a boundary operator $b : \mathcal{E}_s \rightarrow \mathbb{R}^{2N_0+2N_1}$ that extracts the corresponding boundary values of $\bar{\rho}$ and $\bar{\omega}$:

$$b(U) = (\bar{\rho}_{0, j_1} \quad \bar{\rho}_{N_0, j_1} \quad \bar{\omega}_{j_0, 0} \quad \bar{\omega}_{j_0, N_1})$$

and express the boundary conditions as $b(U) = b_0$ where $b_0 = (\rho_0, \rho_1, 0, 0)$, with ρ_0, ρ_1 being the initial and final discrete densities on the centered grid. Note that the above corresponds to imposing Neumann boundary conditions in space. As already mentioned previously, this can be easily adapted to periodic spatial boundary conditions by removing the no-flux constraints and instead applying cyclic index wrapping. We are now just left with the discrete version of the WFR energy and the path equality and inequality constraints. Based on Definition 2.2, for a centered variable $V = (\rho, \omega, \zeta)$, the contribution of each time-space cell $j = (j_0, j_1)$ to the whole WFR cost can be simply taken as $f_\delta(\rho_j, \omega_j, \zeta_j)$. The full cost function is then computed as the discretized time-space integral, i.e.

$$(4.1) \quad J(V) := \sum_{j \in \mathcal{G}_c} f_\delta(\rho_j, \omega_j, \zeta_j) h_0 h_1$$

We note that we use the scaling property [CPSV18a, Proposition 3.1] to reduce the problem to the case $\delta = 1$ if we are given values of δ other than 1. Now, when it comes to the additional path constraints on ρ, ω, ζ , these will be defined on the centered grid via the discretized functions $H_i^\rho, H_i^\omega, H_i^\zeta \in \mathbb{R}^{\mathcal{G}_c}$ for $i = 1, \dots, d$, with d being again the total number of equality and inequality constraints. Slightly departing from the continuous formulation of Section 3, we represent every constraint (inequality and equality) at each time as a box constraint given by the lower and upper bound variables $\ell_i \in \mathbb{R}^{N_0}$ and $u_i \in \mathbb{R}^{N_0}$ with $\ell_i \leq u_i$ component wise. We can then introduce the following constraint operators and constraint sets:

$$\begin{aligned} \mathcal{H}_i(t_{j_0}; V) &:= \langle (H_i^\rho)_{j_0, \cdot}, \rho_{j_0, \cdot} \rangle + \langle (H_i^\omega)_{j_0, \cdot}, \omega_{j_0, \cdot} \rangle + \langle (H_i^\zeta)_{j_0, \cdot}, \zeta_{j_0, \cdot} \rangle, \\ \mathcal{C}_i &:= \{V : \ell_{i, j_0} \leq \mathcal{H}_i(t_{j_0}; V) \leq u_{i, j_0} \quad \forall j_0 \in \llbracket 0, N_0 - 1 \rrbracket\}. \end{aligned}$$

where the bracket notation stands for the discretized L^2 inner product on $[0, L]$, for which we use the simple numerical integration scheme $\langle v, w \rangle = \sum_{j_1=0}^{N_1-1} v_{j_1} w_{j_1} h_1$. Note that since we allow the components of ℓ_i and u_i to take infinite values and be equal to one another, this setting does indeed provide a discrete equivalent of the integral inequality/equality constrained framework developed in Section 3. We finally arrive at the discretized constrained UOT problem, which we formulate as the following optimization program over a pair (U, V) of centered and staggered variables:

$$(4.2) \quad \min_{U, V} J(V) \quad \text{s.t.} \quad (\text{div} - s_z)(U) = 0, \quad b(U) = b_0, \quad V = I(U), \quad V \in \bigcap_{i=1}^d \mathcal{C}_i.$$

Using convex indicator functions for all the constraints, we may rewrite the above as

$$(4.3) \quad \min_{U, V} J(V) + \iota_{\mathcal{CE}}(U) + \iota_{\{V=I(U)\}}(U, V) + \sum_{i=1}^d \iota_{\mathcal{C}_i}(V),$$

where $\mathcal{CE} = \{U : (\text{div} - s_z)(U) = 0, b(U) = b_0\}$. We note that this is a convex problem. Similar to the continuous setting, the existence of minimizers can be guaranteed under the following basic assumption:

THEOREM 4.1. *There exists a minimizer to the discrete constrained WFR problem (4.3) provided that the feasible set is nonempty. Moreover, this condition can be checked by solving a second-order cone feasibility problem.*

We refer the reader to Supplementary Material C.2 for the proof. Similar to the continuous setting and Theorem 3.4, this result ensures the existence of a solution provided that one can find a discrete path with finite energy (4.1) satisfying all constraints, which itself can be verified by solving a second-order cone feasibility problem.

4.2. Algorithmic approach. The Douglas-Rachford splitting algorithm is a generic approach for optimizing the sum of two convex, potentially non-smooth functions. In the context of the present work, having multiple constraints to deal with, we will instead rely on the parallel proximal algorithm (PPXA) [CP08, CP11] which extends the Douglas-Rachford scheme to optimization problems involving the sum of multiple functions. The core idea of PPXA is to rewrite the composite objective function

$$f_1(x) + f_2(x) + \dots + f_m(x)$$

as $F(x_1, \dots, x_m) + \iota_C(x_1, \dots, x_m)$ where $F(x_1, \dots, x_m) = f_1(x_1) + f_2(x_2) + \dots + f_m(x_m)$, $C = \{(x_1, \dots, x_m) | x_1 = x_2 = \dots = x_m\}$, and ι_C is the convex indicator function for this set (as we used in the proof of Theorem 3.4). Thus, one can view the objective function as a sum of two convex functions F and ι_C , and then apply the Douglas-Rachford splitting to this reformulated problem. This approach is called the parallel proximal algorithm (PPXA) [CP08, CP11] since the proximal operators of each f_i can be computed in parallel. We will now describe our main PPXA iteration. Letting $x = (U, V)$ be the current iterate and y_k, π_k auxiliary copies, we group $J + \iota_{C\mathcal{E}}$ as block f_1 , the consistency constraint $\{V = I(U)\}$ as block f_2 , and the d box constraints as the blocks f_3, \dots, f_{d+2} . Then a PPXA step reads

$$\begin{aligned} \pi_1 &= \text{prox}_{\gamma(J + \iota_{C\mathcal{E}})}(y_1), & \pi_2 &= \text{prox}_{\iota_{\{V=I(U)\}}}(y_2), \\ \pi_{i+2} &= \text{prox}_{\iota_{C_i}}(y_{i+2}) \quad \text{for } i = 1, \dots, d, \\ \bar{\pi} &= \frac{1}{d+2} \left(\pi_1 + \pi_2 + \sum_{i=1}^d \pi_{i+2} \right), & y_k &\leftarrow y_k + \alpha (2\bar{\pi} - x - \pi_k), \\ x &\leftarrow x + \alpha (\bar{\pi} - x). \end{aligned}$$

Here, $\alpha \in (0, 2), \gamma > 0$ are hyperparameters. For pseudocode of the full algorithm, see Supplementary Material B.

Remark 4.2 (Convergence). The convergence of our iterations to a minimizer follows from the general theory of the Douglas-Rachford algorithm such as [HY15] assuming the feasibility of the problem since the feasibility implies the existence of a minimizer in the discrete problem (4.3) by Theorem 4.1. In particular, we have the worst-case $O(1/\sqrt{k})$ decay rate for the fixed point residual by the theory in [HY15], where k is the number of iterations or $O(1/k)$ error decay in the ergodic sense as follows from the result of [HY12]. Empirically, as we showcase with the experiments of Section 5.6, we find that the decay rate for the distance from the current to the final iterate is typically sublinear, thus suggesting a potentially faster convergence, in practice, than those theoretical estimates.

Finally, we need to specify how to compute each proximal operator. We note that the calculations for the $\text{prox}_{\gamma(J + \iota_{C\mathcal{E}})}$ and $\text{prox}_{\iota_{\{V=I(U)\}}}$ are exactly the same as in [CPSV18a], so we omit the details here. The new part is the projection onto the (possibly multiple) affine box constraints, which we now describe. For clarity, we shall omit the constraint index i and consider only a single box constraint set:

$$\mathcal{C} = \{V : \ell_{j_0} \leq \mathcal{H}(t_{j_0}; V) \leq u_{j_0} \quad \forall j_0 \in \llbracket 0, N_0 - 1 \rrbracket\}$$

where, for each time index j_0 , $\mathcal{H}(t_{j_0}; V)$ denotes, as in the previous section, the linear functional $V \mapsto \langle H_{j_0, \cdot}^\rho, \rho_{j_0, \cdot} \rangle + \langle H_{j_0, \cdot}^\omega, \omega_{j_0, \cdot} \rangle + \langle H_{j_0, \cdot}^\zeta, \zeta_{j_0, \cdot} \rangle$. Let us also introduce $a_{j_0} := (H^\rho(t_{j_0}, \cdot), H^\omega(t_{j_0}, \cdot), H^\zeta(t_{j_0}, \cdot))$, the spatial weights at t_{j_0} . Since different times have disjoint support, $\{a_{j_0}\}_{j_0}$ form an orthogonal family in the product space \mathcal{E}_c . By [Bau96, Theorem 3.3.14], the projection of V onto \mathcal{C} is given by the orthogonal-box formula, i.e.

$$\text{prox}_{\iota_C}(V) = V - \sum_{j_0=0}^{N_0-1} \frac{\lambda_{j_0}(V)}{\|a_{j_0}\|^2} a_{j_0},$$

$$\lambda_{j_0}(V) = \begin{cases} 0, & \ell_{j_0} \leq \mathcal{H}(t_{j_0}; V) \leq u_{j_0} \\ \mathcal{H}(t_{j_0}; V) - u_{j_0}, & \mathcal{H}(t_{j_0}; V) > u_{j_0} \\ \mathcal{H}(t_{j_0}; V) - \ell_{j_0}, & \mathcal{H}(t_{j_0}; V) < \ell_{j_0}, \end{cases}$$

where $\|a_{j_0}\|^2 = \sum_{j_1=0}^{N_1-1} ((H_{j_0, j_1}^\rho)^2 + (H_{j_0, j_1}^\omega)^2 + (H_{j_0, j_1}^\zeta)^2) h_1$.

5. Numerical experiments. In this section, we demonstrate the capabilities of the proposed framework across various scenarios. These should not be regarded as real-world applications, but rather as simplified examples designed to highlight different aspects of the model. As explained in Remark 3.5 the feasibility (and thus the existence of minimizers) for all examples presented in this section is guaranteed. The experimental

setup and computation timings are detailed in Supplementary Material A. Furthermore, in line with good practices of reproducibility, notebooks for all experiments are publicly available at our GitHub repository <https://github.com/mao1756/acuot>.

5.1. Total mass constraints. As a first example we consider (equality and inequality) constraints on the total mass, which in the setting of (3.1) corresponds to $H^\rho = \pm 1$, $H^\omega = 0$, $H^\zeta = 0$ and a “mass evolution” function $F(t)$.

Spherical Hellinger-Kantorovich distance. We start by discussing the special case of a single equality constraint with $F(t) = 1$, i.e., where ρ_t is constrained to be a probability measure at all times. This situation was first studied by Laschos and Mielke in [LM19] and the derived distance is called the *Spherical Hellinger-Kantorovich distance* (SHK). A deep-learning-based algorithm to compute the solution in this situation was recently proposed in [JCLL24]. Alternatively one can use the results of [LM19, Theorem 2.7], who proved that the unconstrained WFR geometry forms a cone over the SHK geometry. This allows one to obtain the solution of the constrained problem, by projecting the solution from the *unconstrained* problem onto the space of probability densities. We will use this procedure as a benchmark for our constrained implementation. In Figure 1, we show the solution of the SHK optimization problem between two Gaussian bumps. We compare our solution to the projection of the solution to the unconstrained WFR problem using the Laschos-Mielke formula [LM19, Theorem 2.7]. The two solutions agree both qualitatively and quantitatively; the average L^2 distance between these two minimizers is $\approx 3.0 \times 10^{-3}$.

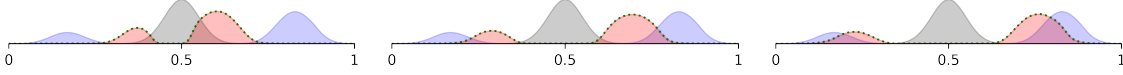


Fig. 1: Spherical Hellinger-Kantorovich distance: Solution of the constrained WFR problem where the solution is restricted to the space of probability measures. Gray and blue indicate ρ_0 and ρ_1 , respectively; the red curves show the solution at $t = 0.25$ (left), $t = 0.5$ (middle), and $t = 0.75$ (right). The green dotted curve represents the solution of the unconstrained WFR geodesic projected onto the constraint according to the results of [LM19].

Inequality constraints on the total mass. Next, let us consider a mass inequality constraint of the form $\int_\Omega d\rho_t(x) \geq c$. For the specific choices of $c = 0.8$ and $c = 1$, Figure 2 shows the solutions where the initial and target densities are again chosen as (shifted) Gaussian bumps. Moreover, we display the total mass of the geodesic at each time t . In this example, we have set the parameter δ in the optimization objective to be small enough ($\delta = 0.5/\pi$) so that destroying and creating mass is on average cheaper than transport.

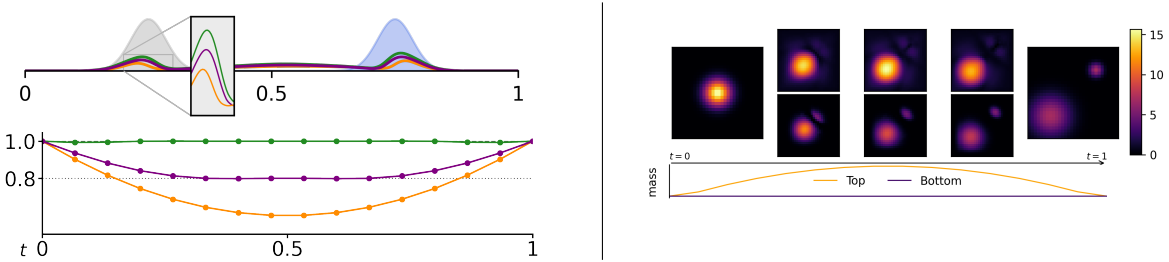


Fig. 2: Left panel: the inequality constraint $\int_\Omega d\rho_t \geq c$, with $c = 0.8$ (purple), $c = 1.0$ (green), and the unconstrained case (orange). Top figure: gray and blue again correspond to ρ_0 and ρ_1 , while the remaining curves display the solution at $t = 0.5$. Bottom figure: Total mass as a function of time for the inequality constraint, with colors matching those in the top figure. Right panel: In 2D, the top panel shows a constrained geodesic and the bottom panel an unconstrained geodesic (evaluated at $t = 0, 0.25, 0.5, 0.75$, and 1.0) along with the evolution of total mass. Here, the total mass constraint is defined by $F(t) = 3 - 8(t - 0.5)^2$ for all $t \in [0, 1]$.

2D total mass constraints. In Figure 2, we also present an example of the WFR problem with total mass equality constraints in 2D. The domain is $[0, 1]^2$, the initial condition is a Gaussian bump at the center, while the terminal distribution is a mixture of two Gaussians. The total mass constraint function is set to $F(t) = 3 - 8(t - 0.5)^2$ so that a solution has to increase mass until $t = 1/2$ and decrease it back after that.

The unconstrained and constrained solutions are shown on the top and bottom row respectively. We observe that the total mass constraint not only influences the total mass of intermediate densities, but also their spatial evolution.

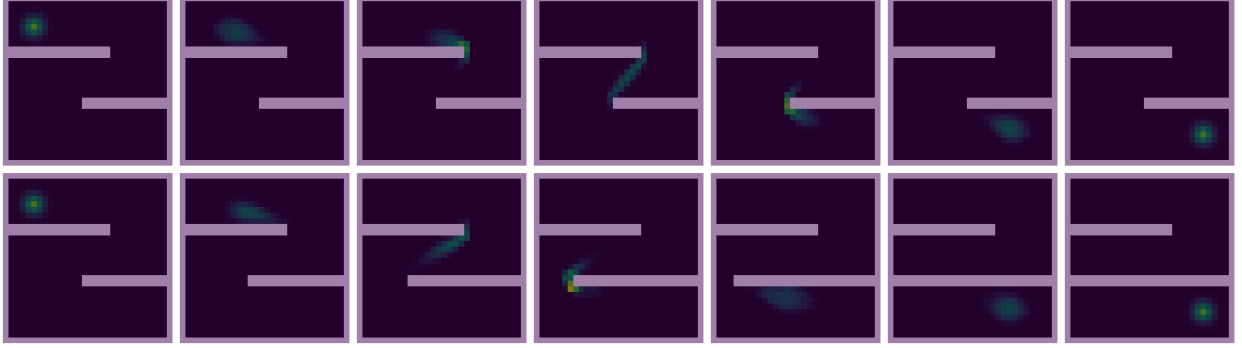


Fig. 3: Barrier constraint: transporting a density through a domain with obstacles. The top row corresponds to a static barrier case, while the bottom one shows the results with a dynamic (i.e. time changing) barrier. The solution is shown at $t = 0, 0.1, 0.3, 0.5, 0.7, 0.9$ and 1.0 .

5.2. Barrier constraints. In this part, we model the situation of (physical) barriers, i.e., specify (possibly time-dependent) regions of the domain in which no mass can enter or be created. This can be implemented as an affine constraint of the form $\int_{\Omega} H(t, x) d\rho_t(x) = 0$, where $H(t, x)$ is a function that is positive in the prohibited region and zero elsewhere. In the following, we present two examples: one with a static barrier and another with a moving barrier. For balanced OT, similar constraints (in the static case) have been previously studied in [PPO14]. Figure 3 displays the solution in these two different scenarios where the initial and final distributions are Gaussian bumps located in the upper left and lower right corners of the 2D domain. For both experiments, we choose a relatively high value for the parameter δ ($\delta = 10$) so as to enforce transport over mass teleportation. In the static case (top row of the figure), we see that the distribution slides along the walls to the target density. For the time-dependent barrier (bottom row), the qualitative behavior is similar but with the notable difference that the motion has to accelerate in the earlier times in order to pass the barrier before it closes off the path.

5.3. Length measures of convex curves. The constraint studied in this section is motivated by convex geometry. The length measure μ of a convex curve in \mathbb{R}^2 is the measure on the unit circle \mathbb{S}^1 defined as the pushforward of its arclength measure by the Gauss map; in other words, for any measurable set $A \subset \mathbb{S}^1$, $\mu(A)$ represents the total length of the portion of the convex curve for which the unit tangent vectors lie within A . Due to a classical theorem of Minkowski [Sch14, Section 8.2.1], μ must satisfy:

$$(5.1) \quad \int_{\mathbb{S}^1} x d\mu(x) = 0.$$

Conversely, if a measure μ on \mathbb{S}^1 satisfies this constraint, then there exists a convex curve, unique up to translations, whose length measure is μ [Sch14, Theorem 8.2.2]. Thus, by considering the WFR energy subject to the constraint (5.1) (i.e. one equality constraint with $H(x) = x$ and $F(t) = 0$), one obtains a corresponding metric on the space of convex curves in \mathbb{R}^2 . For the space of convex, unit length curves, this was considered in [CP21] within the balanced optimal transport setting. Here, we extend this idea to unbalanced optimal transport, thus extending the metric to the space of all convex curves, not only unit length ones. In Figure 4a we show an example, where the source and the target curve (measure, resp.) are both symmetric with respect to the antipodal map $R(x) = -x$, i.e., the source and target measures ρ_0, ρ_1 satisfy $R_*\rho_0 = \rho_0, R_*\rho_1 = \rho_1$ where R_* is the pushforward map by R . In this case, we observe that the unconstrained algorithm leads to essentially the same solution as the constrained algorithm, with the L^2 distance between the constrained and unconstrained solution being 8.7×10^{-8} . This is consistent with the following theoretical result (whose proof is given in Supplementary Material C.3):

LEMMA 5.1. *Let ρ_0, ρ_1 be symmetric with respect to the map $R(x) = -x$. Then, there exists a minimizer of the unconstrained WFR problem between ρ_0 and ρ_1 that is symmetric at almost all times $t \in [0, 1]$. In*

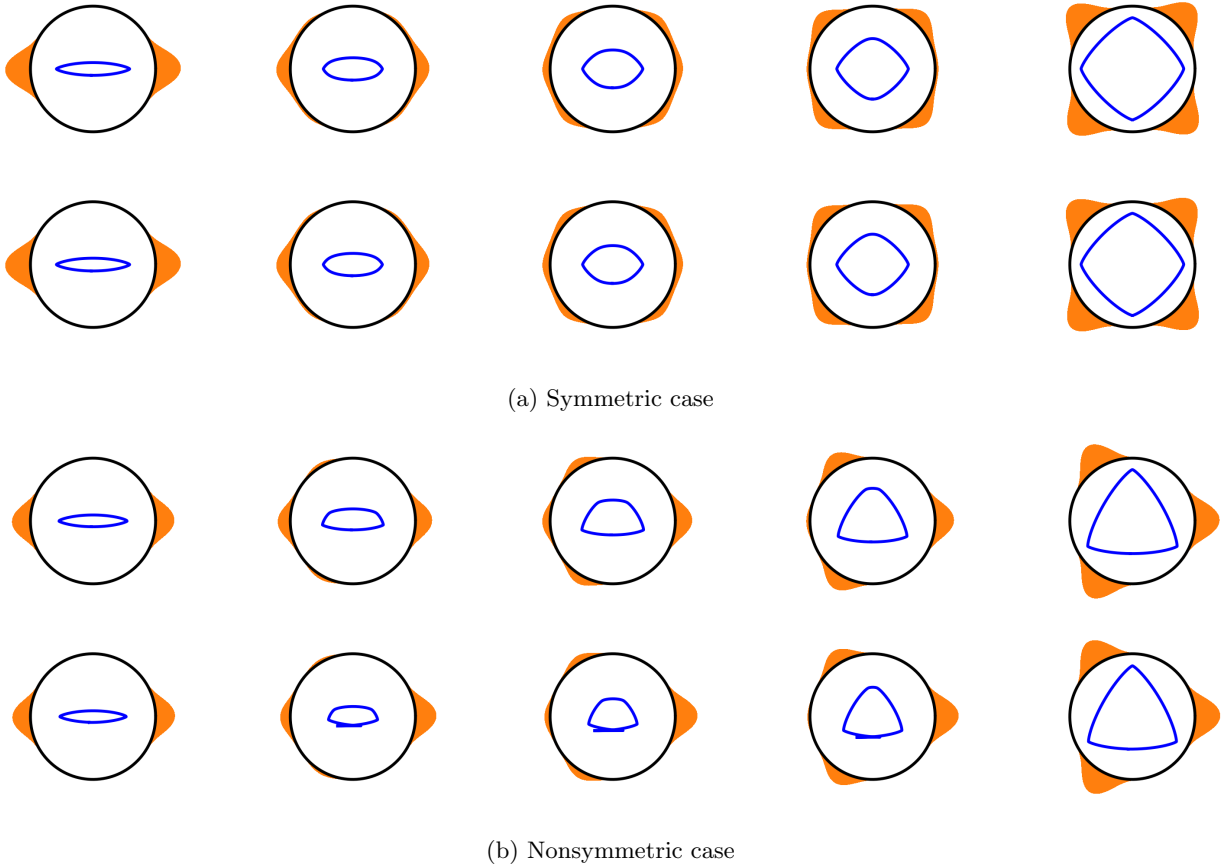


Fig. 4: Effect of a convex-curve constraint on the geodesic evolution. From left to right we show $t = 0, 0.25, 0.5, 0.75$, and 1 . Each panel displays the density on \mathbb{S}^1 (orange) together with the corresponding convex curve (blue). The top row enforces a convex-curve constraint; the bottom row shows the unconstrained geodesic.

particular, this minimizer satisfies the constraint (5.1).

In Figure 4b, we illustrate that for non-symmetric measures, there is, however, a significant difference between the constrained and unconstrained problem. We specifically consider the same initial measure as in our last example, but change the terminal measure to a mixture of three Gaussians on \mathbb{S}^1 , breaking the symmetry w.r.t. the mapping R . We observe that the unconstrained geodesic violates the convex curve constraint, and consequently, the reconstructed interpolating curves are not closed. On the other hand, the constrained geodesic satisfies the convex curve constraint at all times, and thus we obtain a valid interpolation in the space of convex, closed curves. Despite the density plots appearing visually similar, the L^2 distance between the constrained and the unconstrained solution is here 1.3×10^{-1} . We leave it to future work to study more in depth the properties and potential applications of the resulting metric on convex sets, as well as the extension of our numerical framework for convex surfaces and area measures on \mathbb{S}^2 .

5.4. Constraints on control variables. The constraints considered so far only applied to the density path ρ . However, our framework can also handle constraints on the control variables ω and ζ . For instance, one may want to constrain the angle of the momentum ω , or limit the amount of mass created at each time by constraining ζ . In this section, we present two different examples of such constraints.

5.4.1. Momentum flow constraint. In this example, we consider a constraint of the following form:

$$\int_{\Omega} H^{\omega}(t, x) \cdot d\omega_t(x) \geq 0$$

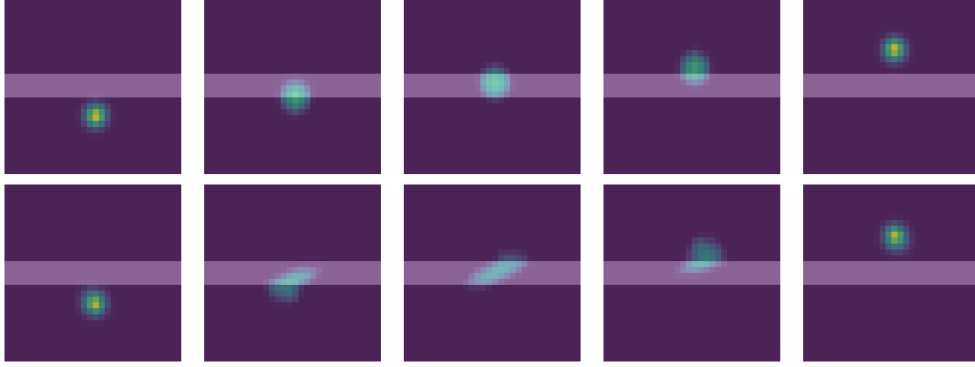


Fig. 5: Illustration of a flow constraint: the brighter region represents where the momentum is constrained to align with the given vector field. The bottom row shows the constrained geodesic, while the top row shows the unconstrained geodesic. Each panel displays the density at $t = 0, 0.25, 0.5, 0.75$, and 1 .

which can be interpreted as enforcing the momentum ω to loosely align with the prescribed vector field $H^\omega(t, x)$, effectively modeling a form of extrinsic current flow such as a river. In Figure 5, we compare transport between localized 2D Gaussian distributions in the constrained and unconstrained settings. For the constrained solution, the vector field $H^\omega(t, x)$ points bottom-right in the purple shaded area and is zero elsewhere. As a result, $\omega(t, x)$ must stay within the halfspace of vectors positively correlated with $H^\omega(t, x)$. Notably, we see that the solution adjusts the momentum direction prior to entering the region as a way to compensate for this effect.

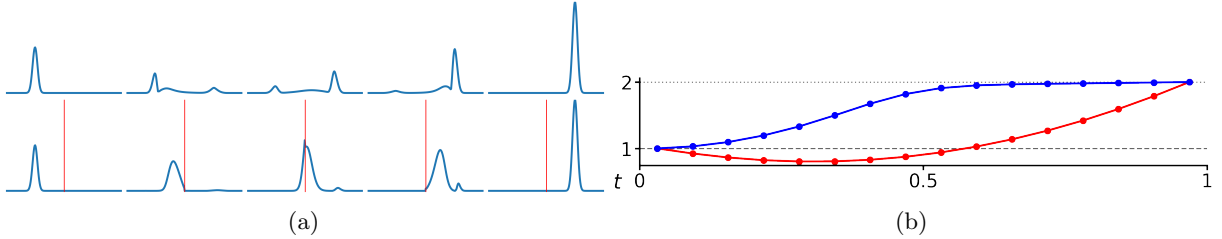


Fig. 6: Panel (a): Budget constraint on mass creation/destruction. The portion to the right of the red line is where the mass creation/destruction is constrained to be small. Top and bottom rows show the unconstrained and constrained solutions, respectively. Each row displays the density at $t = 0, 0.25, 0.5, 0.75$, and 1 . Panel (b): The total mass at each time point for the unconstrained (red) and constrained (blue) optimal paths.

5.4.2. Budget constraint on mass creation/destruction. In this example, we consider a constraint on the source term ζ , of the form:

$$0 \leq \int_{\Omega} H^\zeta(t, x) d\zeta_t(x) \leq C$$

for some constant $C > 0$. This constraint effectively limits the amount of mass that can be created or destroyed at each time, modeling scenarios where resources are limited. In Figure 6a, we compare transport between 1D Gaussian distributions in both constrained and unconstrained settings. For the constrained case, the function $H^\zeta(t, x)$ is set to 1 in the right half of the domain and 0 elsewhere, effectively limiting mass creation/destruction in that region. In this experiment, we set $C = 0.1$. As a result, one can observe that what was mostly a mass creation in the unconstrained model becomes mostly transport in the constrained case. In particular, as evidenced by the total mass plot, the constrained optimal path gradually increases the mass until reaching the constraint region, and maintains a nearly constant mass after that. This example illustrates how constraints on mass creation/destruction can significantly alter the transport dynamics.

5.5. Mixed constraints: population transport. Lastly, in this section, we demonstrate how to impose multiple constraints simultaneously on a real data example. Specifically, we are interested in interpolating between population density maps of the particular county of Ain in France. While we are not

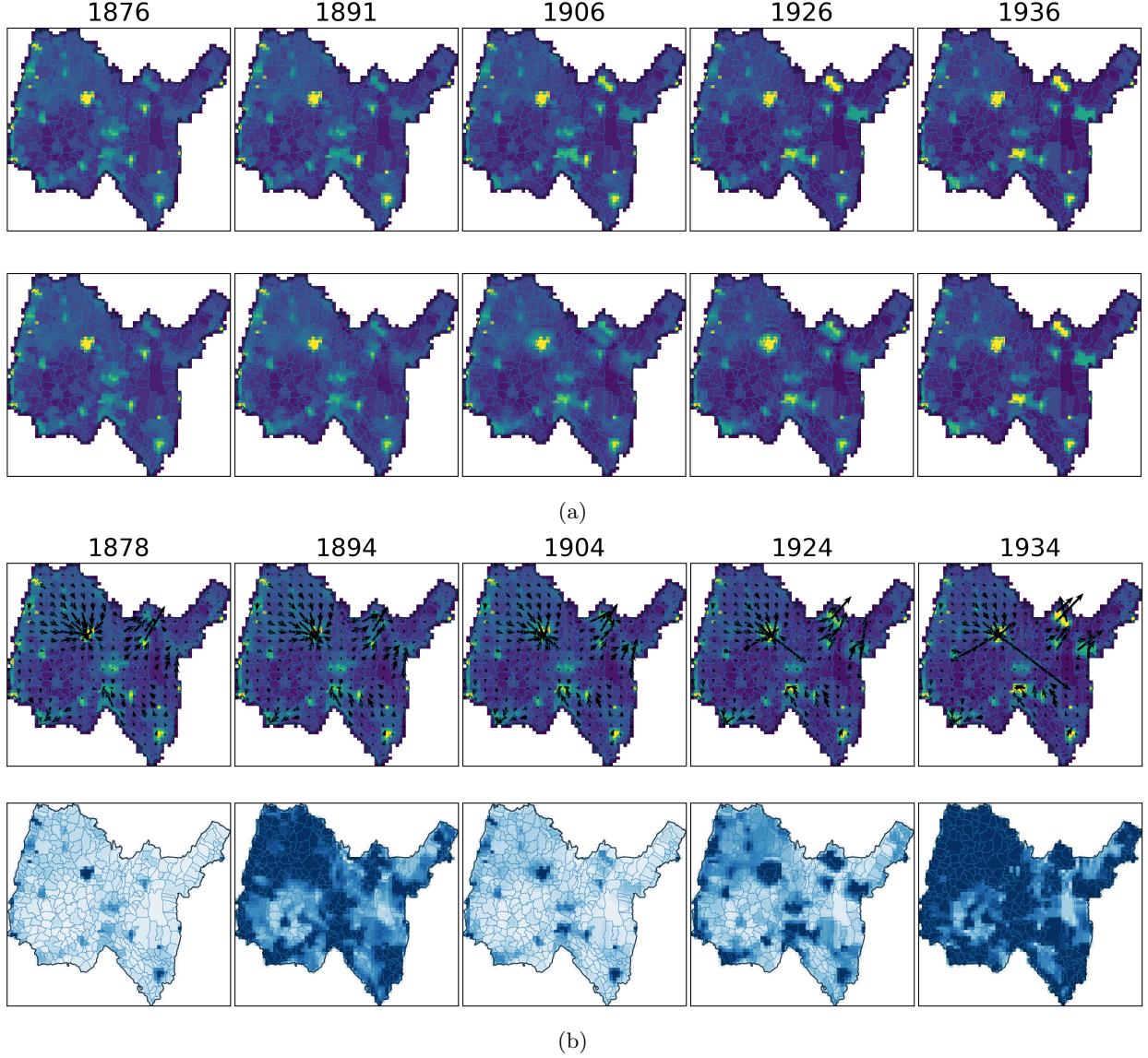


Fig. 7: (a) Population distribution maps of Ain in France, at different years. The top row shows the real data evolution, while the bottom row displays the obtained interpolation between the first (1876) and final year (1936) from our algorithm. Largest discrepancy is observed around the city of Oyonnax (top right), where real data shows a rapid increase in population. (b) Estimated momentum and density values (top) as well as the source term (bottom) across time. The momentum is represented by arrows, with length proportional to the momentum magnitude. The source values have been clipped at the 80th percentile to mitigate the effect of outliers and are represented by color, with darker blue indicating stronger population decrease. Those show population migration towards the cities of Bourg-en-Bresse (center) and Oyonnax (top right). On the other hand, the source term illustrates the important population decrease in rural areas.

claiming that optimal transport is necessarily the proper model for this type of application, this example is mostly here to emphasize how our numerical framework can handle multiple constraints on non-synthetic distributions. Specifically, we consider the population density maps of Ain between the years 1876 and 1936 extracted from the INSEE records [Ins22] (with censuses made at regular five-year intervals), along with the total county population over that period. Our goal is to interpolate between the distributions of 1876 and 1936 and evaluate how the path differs from the ground-truth density evolution. To that end, we impose two types of constraints: a barrier constraint to ensure that the mass remains within the region of interest (Ain) and a total mass constraint enforcing that the total population evolves according to the known records.

Figures 7a and 7b present the population distributions for both the actual data and the optimal interpolation path, as well as the momentum and the source term at various time points. While the general trend of population change is well captured (this particular county witnessed overall population decrease during that period), this approach does not entirely reflect some rapid changes in certain urban areas, such as Oyonnax (top right), between 1906 and 1936. These discrepancies may be attributed to the long time period considered here, which could obscure non-optimal local migration patterns, as well as to the restrictive barrier constraint that excludes in- or out-flows from external regions, among other things.

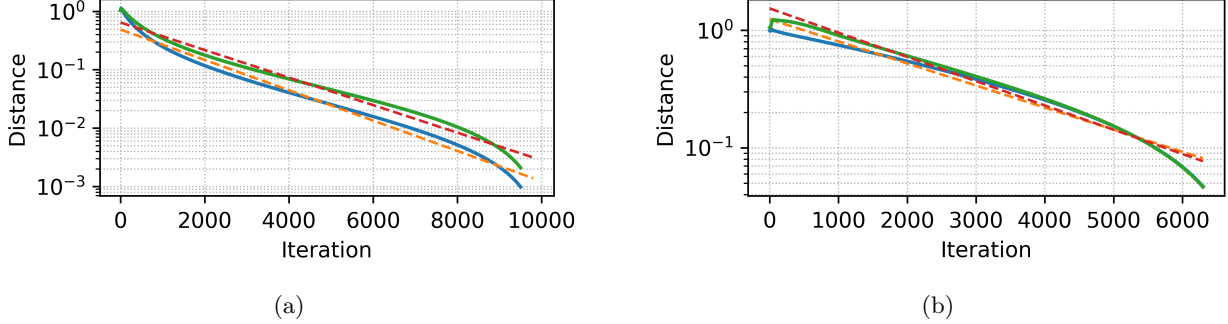


Fig. 8: Convergence plot of the PPXA algorithm. Panel (a) shows the SHK experiment (Section 5.1) while panel (b) shows the static barrier example (Section 5.2). The y -axis shows the relative error between the current iterate and the last iterate (see Algorithm B.1) in the L^2 norm on a log scale. In both figures, the red curves are the obtained linear fits.

5.6. Convergence analysis of the PPXA algorithm. In this final experiment, we seek to examine the convergence rate of the PPXA algorithm. In Figure 8 we present the relative error between the current iterate and the last iterate of the PPXA algorithm for the SHK example (Section 5.1) and the static barrier example (Section 5.2) in the log scale. We have fitted linear curves to the plots that provide good agreement with the empirical convergence rate: for the SHK example we obtained a convergence rate of $q = 0.999414$ for the unconstrained case and $q = 0.999472$ for the constrained case. The corresponding coefficients of determination (the fraction of variance in the data explained by the model) for the linear model were $R^2 = 0.978$ for the unconstrained case and $R^2 = 0.974$ for the constrained case. For the static barrier example, we obtained a convergence rate of $q = 0.999568$ for the unconstrained case and $q = 0.999525$ for the constrained case. Here the corresponding coefficients of determination were $R^2 = 0.966$ for the unconstrained case and $R^2 = 0.979$ for the constrained case. We note that in all these cases the estimated q is very close to one, indicating very slow convergence, e.g. for the SHK example, we need $-1/\log_{10} q \sim 3800$ -4000 iterations to reduce the error by 1 decimal place. Overall, this convergence analysis indicates that while the PPXA algorithm for unbalanced optimal transport problems converges formally geometrically, the rate constant is almost one and thus the practical convergence is rather sublinear. Furthermore, this convergence rate is not significantly affected by the presence of constraints.

6. Conclusions, Future Work and Limitations. In this article we introduced a variant of the dynamic unbalanced optimal transport model which allows one to enforce a set of time-dependent integral equality and inequality constraints along the density, vector field and/or source term paths. This formulation has the important advantage of yielding convex variational problems, with provable conditions of well-posedness in both the continuous and discrete settings. These conditions are still tied to the issue of feasibility (i.e., the existence of finite energy paths satisfying all constraints), for which a more general and systematic study, in the context of our model, remains a subject of possible future work. Based on a discretization over staggered time-space grids, we then proposed an adaptation of the parallel proximal point scheme to tackle the corresponding class of constrained non-smooth optimization problems. We showed empirically, on various examples and constraints, that despite the dimensionality of those problems, the approach is able to estimate an approximate solution in a robust and consistent way. These examples are also meant to illustrate the variety of dynamic constraints that are subsumed under our model, and their potential relevance in different applications. Yet we should also mention a few avenues for further improvement and extension of the framework presented in this paper. A first possible limitation is the specific constraint type

that is considered here. It does not include, for instance, integral convex inequality constraints (beyond affine ones) such as bounds on the entropy or variance of the density ρ_t , or certain forms of congestion constraints in crowd navigation applications [KBAH13, ROL⁺20]. Although these would technically still lead to convex formulations, the generalization of Theorem 3.4 or 4.1 to this new setting is, to our knowledge, not straightforward and thus could be an interesting subject of future investigation. On the numerical side, we expect the PPXA algorithm of Section 4.2 to be still relevant, provided that expressions of the proximal operators for the new constraint functions are available. Another path worth exploring is the extension of the constrained transport model of this paper to the stochastic setting, in particular that of Schrödinger bridge matching and its recent unbalanced version known as generalized Schrödinger bridge matching [LLN⁺24, CGP25], which share many connections to diffusive flows and generative modeling in machine learning.

Acknowledgements. M. Nishino was partially supported by NSF grant CISE-2426549. M. Bauer and T. Needham were partially supported by NSF grants DMS-2324962 and CIF-2526630. N. Charon was partially supported by NSF grants DMS-2438562 and CIF-2526631.

REFERENCES

- [AJVLS17] Nihat Ay, Jürgen Jost, Hồng Vân Lê, and Lorenz Schwachhöfer. *Information geometry*, volume 64. Springer, 2017.
- [Ama16] Shun-ichi Amari. *Information geometry and its applications*, volume 194. Springer, 2016.
- [Bau96] Heinz H. Bauschke. *Projection Algorithms and Monotone Operators*. PhD thesis, Simon Fraser University, Burnaby, BC, Canada, August 1996.
- [BB00] Jean-David Benamou and Yann Brenier. A computational fluid mechanics solution to the Monge-Kantorovich mass transfer problem. *Numerische Mathematik*, 84(3):375–393, January 2000.
- [BBM16] Martin Bauer, Martins Bruveris, and Peter W Michor. Uniqueness of the Fisher–Rao metric on the space of smooth densities. *Bulletin of the London Mathematical Society*, 48(3):499–506, 2016.
- [BCNN25] Martin Bauer, Nicolas Charon, Tom Needham, and Mao Nishino. Path constrained unbalanced optimal transport. *Nonlinearity*, 38(7):075019, 2025.
- [BF20] Kristian Bredies and Silvio Fanzon. An optimal transport approach for solving dynamic inverse problems in spaces of measures. *ESAIM: Mathematical Modelling and Numerical Analysis*, 54(6):2351–2382, nov 2020.
- [BJO09] G. Buttazzo, C. Jimenez, and E. Oudet. An optimization problem for mass transportation with congested dynamics. *SIAM Journal on Control and Optimization*, 48(3):1961–1976, 2009.
- [BZ05] J.M. Borwein and Q.J. Zhu. *Techniques of Variational Analysis*. CMS Books in Mathematics. Springer, 2005.
- [CGP25] Yongxin Chen, Tryphon T Georgiou, and Michele Pavon. Optimal Survival Strategies for Diffusive Flows: A Schrödinger Bridge Approach to Unbalanced Transport. *SIAM Review*, 67(3):579–604, 2025.
- [CP08] Patrick L. Combettes and Jean-Christophe Pesquet. A proximal decomposition method for solving convex variational inverse problems. *Inverse Problems*, 24(6):065014, 2008.
- [CP11] Patrick L. Combettes and Jean-Christophe Pesquet. Proximal splitting methods in signal processing. In Heinz H. Bauschke, Regina S. Burachik, Patrick L. Combettes, Veit Elser, D. Russell Luke, and Henry Wolkowicz, editors, *Fixed-Point Algorithms for Inverse Problems in Science and Engineering*, volume 49 of *Springer Optimization and Its Applications*, pages 185–212. Springer, New York, 2011.
- [CP21] Nicolas Charon and Thomas Pierron. On length measures of planar closed curves and the comparison of convex shapes. *Annals of Global Analysis and Geometry*, 60(4):863–901, November 2021.
- [CPSV18a] Lénaïc Chizat, Gabriel Peyré, Bernhard Schmitzer, and François-Xavier Vialard. An interpolating distance between optimal transport and Fisher–Rao metrics. *Foundations of Computational Mathematics*, 18:1–44, 2018.
- [CPSV18b] Lénaïc Chizat, Gabriel Peyré, Bernhard Schmitzer, and François-Xavier Vialard. Unbalanced optimal transport: Dynamic and Kantorovich formulations. *Journal of Functional Analysis*, 274(11):3090–3123, 2018.
- [DD20] Julie Delon and Agnes Desolneux. A wasserstein-type distance in the space of gaussian mixture models. *SIAM Journal on Imaging Sciences*, 13(2):936–970, 2020.
- [DJH⁺25] Kang Ding, Chunxuan Jiao, Yunze Hu, Kangjie Zhou, Pengying Wu, Yao Mu, and Chang Liu. Swarmdiff: Swarm robotic trajectory planning in cluttered environments via diffusion transformer, 2025.
- [DR56] Jim Douglas and Henry H Rachford. On the numerical solution of heat conduction problems in two and three space variables. *Transactions of the American mathematical Society*, 82(2):421–439, 1956.
- [DS14] Yan Dolinsky and H Mete Soner. Martingale optimal transport and robust hedging in continuous time. *Probability Theory and Related Fields*, 160(1):391–427, 2014.
- [ES18] Ibrahim Ekren and H Mete Soner. Constrained optimal transport. *Archive for Rational Mechanics and Analysis*, 227(3):929–965, 2018.
- [Fol13] G.B. Folland. *Real Analysis: Modern Techniques and Their Applications*. Pure and Applied Mathematics: A Wiley Series of Texts, Monographs and Tracts. Wiley, 2013.
- [Fri91] Thomas Friedrich. Die Fisher-information und symplektische strukturen. *Mathematische Nachrichten*, 153(1):273–296, 1991.
- [FSFC21] Kilian Fatras, Thibault Sèjourné, Rémi Flamary, and Nicolas Courty. Unbalanced minibatch optimal transport;

- applications to domain adaptation. In *International conference on machine learning*, pages 3186–3197. PMLR, 2021.
- [GM75] Roland Glowinski and Americo Marroco. Sur l’approximation, par éléments finis d’ordre un, et la résolution, par pénalisation-dualité d’une classe de problèmes de Dirichlet non linéaires. *Revue française d’automatique, informatique, recherche opérationnelle. Analyse numérique*, 9(R2):41–76, 1975.
- [HY12] Bingsheng He and Xiaoming Yuan. On the $O(1/n)$ Convergence Rate of the Douglas–Rachford Alternating Direction Method. *SIAM Journal on Numerical Analysis*, 50(2):700–709, 2012.
- [HY15] Bingsheng He and Xiaoming Yuan. On the convergence rate of Douglas–Rachford operator splitting method. *Mathematical Programming*, 153(2):715–722, November 2015.
- [Ins22] Insee. Chiffres détaillés — séries historiques de population (1876 à 2020). Excel dataset; geography as of 2022-01-01, 2022. Source: Insee, Recensements de la population.
- [JCLL24] Yang Jing, Jiaheng Chen, Lei Li, and Jianfeng Lu. A machine learning framework for geodesics under spherical wasserstein–fisher–rao metric and its application for weighted sample generation. *Journal of Scientific Computing*, 98(1):5, 2024.
- [KBAH13] Said Kerrache, Hafida Benhidour, and Sahar Al-Homaidhi. An optimal transport-based approach for crowd evacuation. In *2013 Fifth International Conference on Computational Intelligence, Modelling and Simulation*, pages 142–147. IEEE, 2013.
- [KM15] Jonathan Korman and Robert McCann. Optimal transportation with capacity constraints. *Transactions of the American Mathematical Society*, 367(3):1501–1521, 2015.
- [KN22] Said Kerrache and Yasushi Nakauchi. Constrained mass optimal transport. *arXiv preprint arXiv:2206.13352*, 2022.
- [LLN⁺24] Guan Horng Liu, Yaron Lipman, Maximilian Nickel, Brian Karrer, Evangelos A Theodorou, and Ricky TQ Chen. Generalized Schrödinger Bridge Matching. In *12th International Conference on Learning Representations (ICLR)*, 2024.
- [LM19] Vaios Laschos and Alexander Mielke. Geometric properties of cones with applications on the hellinger–kantorovich space, and a new distance on the space of probability measures. *Journal of Functional Analysis*, 276(11):3529–3576, 2019.
- [LMS16] Matthias Liero, Alexander Mielke, and Giuseppe Savaré. Optimal transport in competition with reaction: the Hellinger–Kantorovich distance and geodesic curves. *SIAM Journal on Mathematical Analysis*, 48(4):2869–2911, 2016.
- [LMS18] Matthias Liero, Alexander Mielke, and Giuseppe Savaré. Optimal Entropy–Transport problems and a new Hellinger–Kantorovich distance between positive measures. *Inventiones mathematicae*, 211(3):969–1117, 2018.
- [MRS10] B. Maury, A. Roudneff-Chupin, and F. Santambrogio. A macroscopic crowd motion model of gradient flow type. *Mathematical Models and Methods in Applied Sciences*, 20(10):1787–1821, 2010.
- [MWH⁺21] Zhiheng Ma, Xing Wei, Xiaopeng Hong, Hui Lin, Yunfeng Qiu, and Yihong Gong. Learning to count via unbalanced optimal transport. In *Proceedings of the AAAI Conference on Artificial Intelligence (AAAI)*, volume 35, pages 2319–2327, 2021.
- [NBT⁺24] Kirill Neklyudov, Rob Breckelmans, Alexander Tong, Lazar Atanackovic, Qiang Liu, and Alireza Makhzani. A Computational Framework for Solving Wasserstein Lagrangian Flows. In Ruslan Salakhutdinov, Zico Kolter, Katherine Heller, Adrian Weller, Nuria Oliver, Jonathan Scarlett, and Felix Berkenkamp, editors, *Proceedings of the 41st International Conference on Machine Learning*, volume 235 of *Proceedings of Machine Learning Research*, pages 37461–37485. PMLR, Jul 2024.
- [NNZN23] Quang Minh Nguyen, Hoang H Nguyen, Yi Zhou, and Lam M Nguyen. On unbalanced optimal transport: Gradient methods, sparsity and approximation error. *Journal of Machine Learning Research*, 24(384):1–41, 2023.
- [Ott01] Felix Otto. The Geometry of Dissipative Evolution Equations: The Porous Medium Equation. *Communications in Partial Differential Equations*, 26(1-2):101–174, 2001.
- [PC⁺19] Gabriel Peyré, Marco Cuturi, et al. Computational optimal transport: With applications to data science. *Foundations and Trends® in Machine Learning*, 11(5-6):355–607, 2019.
- [PPO14] Nicolas Papadakis, Gabriel Peyré, and Edouard Oudet. Optimal transport with proximal splitting. *SIAM Journal on Imaging Sciences*, 7(1):212–238, 2014.
- [PR14] Benedetto Piccoli and Francesco Rossi. Generalized wasserstein distance and its application to transport equations with source. *Archive for Rational Mechanics and Analysis*, 211:335–358, 2014.
- [ROL⁺20] Lars Ruthotto, Stanley J Osher, Wuchen Li, Levon Nurbekyan, and Samy Wu Fung. A machine learning framework for solving high-dimensional mean field game and mean field control problems. *Proceedings of the National Academy of Sciences*, 117(17):9183–9193, 2020.
- [RR45] C Radhakrishna Rao. Information and accuracy attainable in the estimation of statistical parameters. *Bulletin of the Calcutta Mathematical Society*, 37(3):81–91, 1945.
- [RW98] R. Tyrrell Rockafellar and Roger J.-B. Wets. *Variational Analysis*, volume 317 of *Grundlehren der mathematischen Wissenschaften*. Springer, Berlin, Heidelberg, 1998.
- [Sch14] Rolf Schneider. *Convex Bodies: The Brunn–Minkowski Theory*, volume 151 of *Encyclopedia of Mathematics and its Applications*. Cambridge University Press, Cambridge, 2nd edition, 2014. Second expanded edition.
- [SFV⁺19] Thibault Séjourné, Jean Feydy, François-Xavier Vialard, Alain Trounev, and Gabriel Peyré. Sinkhorn divergences for unbalanced optimal transport. *arXiv preprint arXiv:1910.12958*, 2019.
- [SST⁺19] Geoffrey Schiebinger, Jian Shu, Marcin Tabaka, Brian Cleary, Vidya Subramanian, Aryeh Solomon, Joshua Gould, Siyan Liu, Stacie Lin, Peter Berube, Lia Lee, Jenny Chen, Justin Brumbaugh, Philippe Rigollet, Konrad Hochedlinger, Rudolf Jaenisch, Aviv Regev, and Eric S. Lander. Optimal-transport analysis of single-cell gene expression identifies developmental trajectories in reprogramming. *Cell*, 176(4):928–943.e22, 2019. Epub

- 2019 Jan 31.
- [TRS⁺24] Xun Tang, Holakou Rahmanian, Michael Shavlovsky, Kiran Koshy Thekumparampil, Tesi Xiao, and Lexing Ying. A sinkhorn-type algorithm for constrained optimal transport. *CoRR*, 2024.
- [Vil09] Cédric Villani. *Optimal transport: old and new*, volume 338. Springer, 2009.
- [WNP⁺23] Michael Wilson, Tom Needham, Chiwoo Park, Suprateek Kundu, and Anuj Srivastava. A Wasserstein-type distance for Gaussian mixtures on vector bundles with applications to shape analysis. *arXiv preprint arXiv:2311.16988*, 2023.
- [WPZ⁺24] Wei Wan, Jiangong Pan, Yuejin Zhang, Chenglong Bao, and Zuoqiang Shi. A neural network framework for high-dimensional dynamic unbalanced optimal transport. *arXiv preprint arXiv:2409.13188*, 2024.
- [WR24] Dongjun Wu and Anders Rantzer. Optimal mass transport of nonlinear systems under input and density constraints. 2024.
- [WSZJ24] Zifan Wang, Yi Shen, Michael M. Zavlanos, and Karl Henrik Johansson. Outlier-robust distributionally robust optimization via unbalanced optimal transport. In *The Thirty-eighth Annual Conference on Neural Information Processing Systems*, 2024.
- [WZB⁺23] Wei Wan, Yuejin Zhang, Chenglong Bao, Bin Dong, and Zuoqiang Shi. A Scalable Deep Learning Approach for Solving High-Dimensional Dynamic Optimal Transport. *SIAM Journal on Scientific Computing*, 45(4):B544–B563, 2023.

Supplementary Material A. Experimental Details.

A.1. Environment.

OS: Windows 11 Pro (Build 26100).

Software stack: Python <3.12.7>; numpy <2.1.3>; scipy <1.14.1>; POT <0.9.5>.

A.2. Hardware.

System: Dell G15 5530 laptop (x64).

CPU: Intel Core i7-13650HX (20 CPUs), ~ 2.6 GHz.

Memory: 16 GB RAM.

A.3. Hyperparameters. The global hyperparameters used in all experiments are as follows:

- Relaxation parameter: $\alpha = 1.8$.
- Proximal parameter: $\gamma = \max(\max(\rho_0), \max(\rho_1))/2$ where ρ_0 and ρ_1 are the initial and terminal densities.

These choices are inherited from the code for the unconstrained case by [CPSV18a] and have been found to work well in practice. For each experiment, we also have specific hyperparameters, which are summarized in Table 1.

Experiment	T	Space grid size	#iter	δ
SHK	15	(256,)	10000	1.0
Inequality total mass	15	(256,)	3000	$\frac{1}{2\pi}$
2D total mass	15	(30, 30)	3000	1.0
Static barrier	30	(30, 30)	7000	10.0
Moving barrier	30	(30, 30)	7000	10.0
French population	12	(64, 64)	10000	1.0
Symmetric curve	15	(256,)	10000	0.01
Nonsymmetric curve	15	(256,)	10000	0.01
River	15	(30, 30)	3000	2.0
Budget	15	(256,)	3000	$\frac{1}{2\pi}$

Table 1: Hyperparameters for each experiment. Here, T is the number of time steps, #iter is the number of iterations, and δ is the interpolation parameter between transport and Fisher-Rao terms in the WFR energy.

A.4. Wall-clock times. The wall-clock times for each experiment are summarized in Table 2. All experiments were run on a single CPU core. The time is only for the optimization algorithm, excluding the time for data loading and visualization.

Supplementary Material B. Pseudocode of the PPXA Implementation of Constrained UOT.

Experiment	Mean time (sec) \pm std. dev.
SHK	22.025 \pm 0.424
Inequality total mass	7.400 \pm 0.320
2D total mass	23.359 \pm 0.621
Static barrier	115.066 \pm 3.094
Moving barrier	114.071 \pm 2.726
French population	425.274 \pm 24.554
Symmetric curve	24.916 \pm 0.184
Nonsymmetric curve	24.577 \pm 0.067
River	26.738 \pm 0.426
Budget	6.762 \pm 0.016

Table 2: Wall-clock times for each experiment. The mean is computed over 3 runs.

Algorithm B.1 PPXA for constrained WFR geodesics with M box constraints

```

1: Input:  $\rho_0, \rho_1$ , grid sizes  $N_0, \dots, N_d$ , lengths  $L_1, \dots, L_d$ .
2: Constraints: For each  $m = 1, \dots, M$ , weights  $H_{\bullet}^{(m)}$  and bounds  $(\ell^{(m)}, u^{(m)})$ .
3: Initialize  $(U, V)$  (linear or Fisher–Rao path for  $\rho$ ); set  $y_1 = \dots = y_{2+M} = (U, V)$ .
4: Set  $\pi_k = (U, V)$  for  $k = 1, \dots, 2 + M$ .
5: for  $n = 0, 1, \dots, n_{\max} - 1$  do
6:    $\pi_1 \leftarrow \text{prox}_{\gamma(J+\iota_{\mathcal{CE}})}(y_1)$   $\triangleright$  pointwise WFR prox on  $V$  + CE projection on  $U$ 
7:    $\pi_2 \leftarrow \text{prox}_{\iota_{\{V=I(U)\}}}(y_2)$   $\triangleright$  projection onto  $V = I(U)$ 
8:   for  $m = 1$  to  $M$  do
9:      $\pi_{m+2} \leftarrow \text{prox}_{\iota_{\mathcal{C}(m)}}(y_{m+2})$   $\triangleright$  affine box projection (constraint  $m$ )
10:  end for
11:   $\bar{\pi} \leftarrow (\pi_1 + \pi_2 + \sum_{m=1}^M \pi_{m+2}) / (2 + M)$ 
12:   $y_k \leftarrow y_k + \alpha(2\bar{\pi} - (U, V) - \pi_k)$  for  $k = 1, \dots, 2 + M$ 
13:   $(U, V) \leftarrow (U, V) + \alpha(\bar{\pi} - (U, V))$ 
14: end for
15: Return  $(U, V)$  with either  $\bar{\rho}$  or  $\rho$  as the geodesic where  $U = (\bar{\rho}, \bar{\omega}, \bar{\zeta})$  or  $V = (\rho, \omega, \zeta)$ .
```

Supplementary Material C. Mathematical Proofs.**C.1. Proof of Theorem 3.4.**

Proof of Theorem 3.4. Toward applying the Fenchel-Rockafellar theorem, we start by introducing the following Banach spaces X and Y :

$$\begin{aligned}
X &= C^1([0, 1] \times \Omega) \times C([0, 1])^d, \\
Y &= C([0, 1] \times \Omega) \times C([0, 1] \times \Omega)^n \times C([0, 1] \times \Omega).
\end{aligned}$$

We define the convex function $\mathcal{F} : Y \rightarrow \mathbb{R} \cup \{+\infty\}$ by

$$\mathcal{F}(\alpha, \beta, \gamma) = \int_{[0,1] \times \Omega} \iota_{B_\delta}(\alpha(t, x), \beta(t, x), \gamma(t, x)) dt dx,$$

where $\iota_{B_\delta} : \mathbb{R} \times \mathbb{R}^n \times \mathbb{R} \rightarrow \mathbb{R} \cup \{+\infty\}$ is the convex indicator function of the set B_δ , defined by

$$B_\delta = \left\{ (a, b, c) \in \mathbb{R} \times \mathbb{R}^n \times \mathbb{R} \left| a + \frac{1}{2} \left(\|b\|^2 + \frac{c^2}{\delta^2} \right) \leq 0 \right. \right\};$$

that is, $\iota_{B_\delta}(a, b, c) = 0$ if $(a, b, c) \in B_\delta$, and is otherwise equal to $+\infty$. The Fenchel conjugate of ι_{B_δ} is the

Wasserstein-Fisher-Rao infinitesimal cost f_δ . Next, we define a function $\mathcal{G} : X \rightarrow \mathbb{R} \cup \{+\infty\}$ by

$$\begin{aligned} \mathcal{G}(\phi, \psi) &= - \sum_{i=1}^{d'} \int_0^1 \psi_i(t) (F_i(t)) dt + \iota_{s \leq 0} \left(\sup_{t \in [0,1]} \psi'(t) \right) \\ &\quad - \sum_{i=d'+1}^d \int_0^1 \psi_i(t) F_i(t) dt + \int_{\Omega} \phi(0, \cdot) d\rho_0 - \int_{\Omega} \phi(1, \cdot) d\rho_1. \end{aligned}$$

where:

- $\psi' = (\psi_1, \dots, \psi_{d'}) \in C([0, 1])^{d'}$,
- $\iota_{s \leq 0}$ is the convex indicator of the nonpositive orthant of $\mathbb{R}^{d'}$, i.e.,

$$\iota_{s \leq 0}(x_1, \dots, x_d) = \begin{cases} 0 & \text{if } x_i \leq 0 \ \forall i = 1, \dots, d \\ +\infty & \text{otherwise;} \end{cases}$$

- $\sup_{t \in [0,1]} \psi'(t) \in \mathbb{R}^{d'}$ denotes the coordinate-wise supremum over the interval $[0, 1]$.

We point out that \mathcal{G} is a convex function over X . As the last step in setting up the Fenchel-Rockafellar theorem, let $A : X \rightarrow Y$ be the bounded linear operator defined by

$$A(\phi, \psi) = \left(\partial_t \phi + \sum_{i=1}^d H_i^\rho \psi_i, \nabla \phi + \sum_{i=1}^d H_i^\omega \psi_i, \phi + \sum_{i=1}^d H_i^\zeta \psi_i \right).$$

We then consider the primal problem

$$(C.1) \quad \inf_{x \in X} \mathcal{F}(Ax) + \mathcal{G}(x).$$

Using a similar argument as in the proof of [BCNN25, Theorem 4.3], one easily checks that there exists $x_0 \in X$ that satisfies the conditions of Fenchel-Rockafellar strong duality theorem—namely, $\mathcal{G}(x_0), \mathcal{F}(Ax_0) < +\infty$ and \mathcal{F} is continuous at Ax_0 —so that (C.1) is equivalent to the Lagrange dual problem:

$$(C.2) \quad \sup_{y^* \in Y^*} -\mathcal{F}^*(y^*) - \mathcal{G}^*(-A^*y^*).$$

Using [Fol13, Theorem 7.17], we can identify the dual Y^* as

$$Y^* \approx \mathcal{M}([0, 1] \times \Omega) \times \mathcal{M}([0, 1] \times \Omega)^n \times \mathcal{M}([0, 1] \times \Omega),$$

Following the argument of [CPSV18a], $\mathcal{F}^*(y^*)$ is equal to the objective function of the constrained Wasserstein-Fisher-Rao problem (3.1). We will show that the second term of (C.2) enforces the constraints of (3.1), which then proves the theorem, as the Fenchel-Rockafellar theorem guarantees the existence of a maximizer in (C.2), hence of a minimizer for (3.1). It remains to understand the second term of (C.2). We have

$$(C.3) \quad \mathcal{G}^*(-A^*y^*) = \sup_{x=(\phi, \psi) \in X} \{ \langle -A^*y^*, x \rangle - \mathcal{G}(x) \} = \sup_{x \in X} \{ -\langle y^*, Ax \rangle - \mathcal{G}(x) \}.$$

Moreover, we have by definition that

$$\begin{aligned} \langle y^*, Ax \rangle &= \int_{[0,1] \times \Omega} \partial_t \phi d\rho + \int_{[0,1] \times \Omega} \nabla \phi \cdot d\omega + \int_{[0,1] \times \Omega} \phi d\zeta \\ &\quad + \sum_{i=1}^d \int_{[0,1] \times \Omega} \psi_i H_i^\rho d\rho + \sum_{i=1}^d \int_{[0,1] \times \Omega} \psi_i H_i^\omega \cdot d\omega + \sum_{i=1}^d \int_{[0,1] \times \Omega} \psi_i H_i^\zeta d\zeta, \end{aligned}$$

from which we deduce that $\mathcal{G}^*(-A^*y^*)$ can be expressed as the sum of three terms:

$$(C.4) \quad \sup_{\phi} \left\{ - \int_{[0,1] \times \Omega} \partial_t \phi d\rho - \int_{[0,1] \times \Omega} \nabla \phi \cdot d\omega \right. \\ \left. - \int_{[0,1] \times \Omega} \phi d\zeta + \int_{\Omega} \phi(1, \cdot) d\rho_1 - \int_{\Omega} \phi(0, \cdot) d\rho_0 \right\},$$

$$(C.5) \quad \sum_{i=1}^{d'} \sup_{\psi_i \leq 0} \int_0^1 \psi_i(t) \left(F_i(t) - \int_{\Omega} H_i^{\rho} d\rho_t - \int_{\Omega} H_i^{\omega} \cdot d\omega_t - \int_{\Omega} H_i^{\zeta} d\zeta_t \right) dt,$$

and

$$(C.6) \quad \sum_{i=d'+1}^d \sup_{\psi_i} \int_0^1 \psi_i(t) \left(F_i(t) - \int_{\Omega} H_i^{\rho} d\rho_t - \int_{\Omega} H_i^{\omega} \cdot d\omega_t - \int_{\Omega} H_i^{\zeta} d\zeta_t \right) dt.$$

We now describe the properties of each term. The first sup over ϕ (C.4) is zero when $\mu = (\rho, \omega, \zeta)$ satisfies the continuity equation and $+\infty$ otherwise. This term therefore enforces the continuity equation in the supremum (C.2). To get the second term (C.5), we have used the presence of the indicator function $\iota_{s \leq 0} \left(\sup_{t \in [0,1]} \psi'(t) \right)$ in \mathcal{G} to deduce that, when taking the supremum in (C.3), one can restrict to functions which satisfy $\psi_i(t) \leq 0$ for a.e. $t \in [0, 1]$ and for all $i = 1, \dots, d'$. Now suppose that the inequality constraint

$$\int_{\Omega} H_i^{\rho} d\rho_t + \int_{\Omega} H_i^{\omega} \cdot d\omega_t + \int_{\Omega} H_i^{\zeta} d\zeta_t \leq F_i(t) \quad (\text{for a.e. } t \in [0, 1])$$

is satisfied. Then the term in parentheses in (C.5) is non-negative, hence the supremum over ψ_i 's satisfying $\psi_i \leq 0$ is zero. On the other hand, if the inequality constraint fails, then the term in parentheses is negative on a set of positive measure, hence ψ_i 's may be chosen to make (C.5) arbitrarily large. Putting this together, we have that the inequality constraint is enforced by the term (C.5). Lastly, it is straightforward to show that the term (C.6) is equal to zero when the equality constraints $\mu \in \mathcal{A}^{\text{eq}}(H_i, F_i)$ hold for $i = d' + 1, \dots, d$ and $+\infty$ otherwise. Putting all of our observations together, we deduce that

$$\mathcal{G}^*(-A^*y^*) = \begin{cases} 0 & \text{if } (\rho, \omega, \zeta) \in \mathcal{CE}_{H,F}(\rho_0, \rho_1) \\ +\infty & \text{otherwise.} \end{cases}$$

This finally allows us to recover that the dual problem is equivalent to (3.1) and that, by Fenchel-Rockafellar strong duality, the two problems have the same optimal value and that there exists a dual optimal that is therefore a solution of the constrained unbalanced optimal transport problem. \square

C.2. Proof of Theorem 4.1. Our proof will rely on the following intermediate result involving the notion of the horizon cone [RW98, Definition 3.3]:

PROPOSITION C.1. *Let V, W be finite dimensional normed vector spaces, $L : V \rightarrow W$ be a linear map and $w \in W$. Let $C = \{v \in V : Lv = w\}$ be an affine subspace of V . Then, the horizon cone of C is the kernel of L i.e. $C^\infty = \ker(L)$.*

Proof. Since C is convex and closed, by Theorem 3.6 of [RW98], we have $C^\infty = \{y \in V : \exists x \in C, \forall t \geq 0, x + ty \in C\}$. Let $y \in C^\infty$, then there exists $x \in C$ and for all $t \geq 0$, we have $L(x + ty) = w + tLy = w$. This implies that $Ly = 0$ i.e. $y \in \ker(L)$. Conversely, if $y \in \ker(L)$, then for any $x \in C$ and $t \geq 0$, we have $L(x + ty) = Lx + tLy = w + 0 = w$. This implies that $x + ty \in C$ and thus $y \in C^\infty$. Therefore, we have shown that $C^\infty = \ker(L)$. \square

We now move to the main proof of Theorem 4.1:

Proof of Theorem 4.1. Let us first rewrite the objective function:

$$F(U, V) = J(V) + \iota_{\mathcal{CE}}(U) + \iota_{\{V=I(U)\}}(U, V) + \sum_{i=1}^d \iota_{C_i}(V)$$

The main element of the proof is to show that the horizon function [RW98, Definition 3.17] of F , denoted F^∞ in the following, is zero only when $U = 0, V = 0$. This will imply that F is level-bounded by [RW98, Theorem 3.26(a), Corollary 3.27] since F is proper, convex and lower semicontinuous. (Note that properness of F i.e. that $F(U, V) < \infty$ for some U, V , follows from the feasibility assumption.) The existence of minimizers then follows from the fact that a lower-semicontinuous proper and level-bounded function attains a finite minimum

[RW98, Theorem 1.9]. By the sum property of the horizon functions [RW98, Exercise 3.29], and the fact that $\iota_C^\infty = \iota_{C^\infty}$, we have:

$$\begin{aligned} F^\infty &\geq J^\infty + \iota_{\mathcal{CE}}^\infty + \iota_{\{V=I(U)\}}^\infty + \sum_{i=1}^d \iota_{\mathcal{C}_i}^\infty \\ &\geq J^\infty + \iota_{\mathcal{CE}^\infty} + \iota_{\{V=I(U)\}^\infty} \end{aligned}$$

Note that $J^\infty = J$ since f_δ is positively homogeneous. Now, if $F^\infty(U, V) = 0$, then we must have $J(V) = 0$, $(U, V) \in \mathcal{CE}^\infty$, $(U, V) \in \{(U, V) | V = I(U)\}^\infty$. If we write $V = (\rho, \omega, \zeta)$, the definition of f_δ implies that $J(V) = 0$ only when $\omega = \zeta = 0$. Now, by Proposition C.1, we have

$$\begin{aligned} \mathcal{CE}^\infty &= \{(\rho, \omega, \zeta) : (\operatorname{div} - s_z)(U) = 0, b(U) = 0\} \\ \{(U, V) | V = I(U)\}^\infty &= \{(U, V) : V = I(U)\} \end{aligned}$$

If we write $U = (\bar{\rho}, \bar{\omega}, \bar{\zeta})$, the condition $(U, V) \in \{(U, V) | V = I(U)\}$ implies that $\zeta = 0$ too. Moreover, we must have $\bar{\omega}_{j_0, j_1+1} = -\bar{\omega}_{j_0, j_1}$ for all $j_0 \in \llbracket 0, N_0 - 1 \rrbracket$, $j_1 \in \llbracket 0, N_1 - 1 \rrbracket$. On the other hand, since we must have $b(U) = 0$, we have $\bar{\omega}_{j_0, 0} = \bar{\omega}_{j_0, N_1} = 0$ for all $j_0 \in \llbracket 0, N_0 - 1 \rrbracket$. This implies that $\bar{\omega} = 0$. Finally, the condition $(\operatorname{div} - s_z)(U) = 0$, together with $\bar{\omega} = 0, \bar{\omega} = 0$, implies that

$$\frac{\bar{\rho}_{j_0+1, j_1} - \bar{\rho}_{j_0, j_1}}{h_0} = 0 \text{ for all } j_0 \in \llbracket 0, N_0 - 1 \rrbracket, j_1 \in \llbracket 0, N_1 - 1 \rrbracket$$

Together with the boundary condition $b(U) = 0$, this implies that $\bar{\rho} = 0$. $V = I(U)$ then implies that $\rho = 0$. Overall, we have $U = 0, V = 0$. Therefore, we have shown that $F^\infty(U, V) = 0$ only when $U = 0, V = 0$. This concludes the proof of solution's existence. Now, regarding the feasibility condition, we see that (U, V) belongs to the feasible set of problem (4.2) if and only if it satisfies the set of conditions $(\operatorname{div} - s_z)(U) = 0$, $b(U) = b_0$, $V = I(U)$ and $V \in \cap_{i=1}^d \mathcal{C}_i$, which are all affine equality and inequality constraints, and the condition that the energy $J(V) < +\infty$. The latter translates to $\rho_j > 0$ or $(\rho_j, \omega_j, \zeta_j) = (0, 0, 0)$ for any $j = (j_0, j_1) \in \mathcal{G}_c$. This is equivalent to the existence of $\tau \geq 0$ such that for all j , $\|(\omega_j, \delta\zeta_j)\|_2^2 \leq 2\tau\rho_j$. Indeed, one can take τ to be the largest of the $\frac{\|(\omega_j, \delta\zeta_j)\|_2^2}{2\rho_j}$ over all j such that $\rho_j > 0$. We can rewrite each of these conditions as follows:

$$\begin{aligned} \|(\omega_j, \delta\zeta_j)\|_2^2 \leq 2\tau\rho_j &= (\tau + \rho_j)^2 - \tau^2 - \rho_j^2 \Leftrightarrow \|(\omega_j, \delta\zeta_j)\|_2^2 + \tau^2 + \rho_j^2 \leq (\tau + \rho_j)^2 \\ &\Leftrightarrow \|(\rho_j, \omega_j, \delta\zeta_j, \tau)\|_2^2 \leq (\tau + \rho_j)^2 \end{aligned}$$

which is in turn equivalent to $\|(\rho_j, \omega_j, \delta\zeta_j, \tau)\|_2 \leq \tau + \rho_j$. Thus, the feasibility set of the problem can be expressed as an intersection of hyperplanes, halfspaces and second-order cone conditions on $(\rho, \omega, \zeta, \tau)$. \square

C.3. Proof of Lemma 5.1.

Proof. From the results of [CPSV18a], there exists a minimizer (ρ, ω, ζ) to the standard WFR problem where $\rho, \omega, \zeta \in \mathcal{M}([0, 1] \times \mathbb{S}^1)$. With Propositions 2.2 and 2.6 of [BF20], we can further assume that all three measures are disintegrable in time with respect to the Lebesgue measure. Let us then define the following:

$$\begin{aligned} \bar{\rho} &= \frac{1}{2}(\rho_t + R_*\rho_t) \otimes dt \\ \bar{\omega} &= \frac{1}{2}(\omega_t + R_*\omega_t) \otimes dt \\ \bar{\zeta} &= \frac{1}{2}(\zeta_t + R_*\zeta_t) \otimes dt. \end{aligned}$$

where dt represents the Lebesgue measure on $[0, 1]$ and \otimes represents the disintegration of measure. Due to

the symmetry of ρ_0 and ρ_1 , we see that $\bar{\rho}_0 = \rho_0$ and $\bar{\rho}_1 = \rho_1$. In addition, for every $\phi \in \mathcal{C}^1([0, 1] \times \mathbb{S}^1)$,

$$\begin{aligned} & \int_{[0,1] \times \mathbb{S}^1} \partial_t \phi d\bar{\rho} + \int_{[0,1] \times \mathbb{S}^1} \partial_\theta \phi d\bar{\omega} + \int_{[0,1] \times \mathbb{S}^1} \phi d\bar{\zeta} \\ &= \frac{1}{2} \left(\int_{[0,1] \times \mathbb{S}^1} \partial_t \phi d\rho + \int_{[0,1] \times \mathbb{S}^1} \partial_\theta \phi d\omega + \int_{[0,1] \times \mathbb{S}^1} \phi d\zeta \right) \\ &+ \frac{1}{2} \left(\int_0^1 \int_{\mathbb{S}^1} \partial_t \phi d(R_* \rho_t) dt + \int_0^1 \int_{\mathbb{S}^1} \partial_\theta \phi d(R_* \omega_t) dt + \int_0^1 \int_{\mathbb{S}^1} \phi d(R_* \zeta_t) dt \right). \end{aligned}$$

By assumption the upper term equals to $\frac{1}{2} (\int_{\mathbb{S}^1} \phi(1, \cdot) d\rho_1 - \int_{\mathbb{S}^1} \phi(0, \cdot) d\rho_0)$. By a change of variable in the inner integrals, writing $\bar{\phi}(t, \theta) = \phi(t, \theta + \pi)$, we obtain that the second term becomes:

$$\begin{aligned} & \frac{1}{2} \left(\int_0^1 \int_{\mathbb{S}^1} \partial_t \bar{\phi} d\rho_t dt + \int_0^1 \int_{\mathbb{S}^1} \partial_\theta \bar{\phi} d\omega_t dt + \int_0^1 \int_{\mathbb{S}^1} \bar{\phi} d\zeta_t dt \right) \\ &= \frac{1}{2} \left(\int_{\mathbb{S}^1} \bar{\phi}(1, \cdot) d\rho_1 - \int_{\mathbb{S}^1} \bar{\phi}(0, \cdot) d\rho_0 \right) = \frac{1}{2} \left(\int_{\mathbb{S}^1} \phi(1, \cdot) d\rho_1 - \int_{\mathbb{S}^1} \phi(0, \cdot) d\rho_0 \right) \end{aligned}$$

where the last equality follows from the fact that ρ_0 and ρ_1 are symmetric. It results that $(\bar{\rho}, \bar{\omega}, \bar{\zeta})$ satisfy the continuity equation. Furthermore, for a.e. $t \in [0, 1]$, letting λ_t be a measure such that $\bar{\rho}_t, \bar{\omega}_t, \bar{\zeta}_t \ll \lambda_t$, we have:

$$\begin{aligned} & \int_0^1 \int_{\mathbb{S}^1} f_\delta \left(\frac{d\bar{\rho}_t}{d\lambda_t}, \frac{d\bar{\omega}_t}{d\lambda_t}, \frac{d\bar{\zeta}_t}{d\lambda_t} \right) d\lambda_t dt \\ & \leq \frac{1}{2} \int_0^1 \int_{\mathbb{S}^1} f_\delta \left(\frac{d\rho_t}{d\lambda_t}, \frac{d\omega_t}{d\lambda_t}, \frac{d\zeta_t}{d\lambda_t} \right) d\lambda_t dt + \frac{1}{2} \int_0^1 \int_{\mathbb{S}^1} f_\delta \left(\frac{dR_* \rho_t}{d\lambda_t}, \frac{dR_* \omega_t}{d\lambda_t}, \frac{dR_* \zeta_t}{d\lambda_t} \right) d\lambda_t dt \end{aligned}$$

which follows from the convexity of the function f_δ . Note finally that, due to the invariances of the cost function, $(R_* \rho_t, R_* \omega_t, R_* \zeta_t) \otimes dt$ must be a minimizer for the WFR_δ distance between $R_* \rho_0 = \rho_0$ and $R_* \rho_1 = \rho_1$, and as a consequence both terms are equal to $\text{WFR}_\delta(\rho_0, \rho_1)^2/2$. We thus get that:

$$\int_0^1 \int_{\mathbb{S}^1} f_\delta \left(\frac{d\bar{\rho}_t}{d\lambda_t}, \frac{d\bar{\omega}_t}{d\lambda_t}, \frac{d\bar{\zeta}_t}{d\lambda_t} \right) d\lambda_t dt \leq \text{WFR}_\delta(\rho_0, \rho_1)^2$$

and thus $t \mapsto \bar{\rho}_t$ is a geodesic between ρ_0 and ρ_1 and is symmetric at all times. \square